

Clapping propulsion and thin vortex rings: a computational study of vortex dynamics, energy equivalence, and core potential energy

Suyog Mahulkar^{1†}, Jaywant Arakeri¹

¹Indian Institute of Science, Bangalore, India

(Received xx; revised xx; accepted xx)

We present a numerical study on clapping propulsion using a body consisting of two rigid plates hinged at one end, with a 60° interplate cavity. The closing of the cavity generates a thrust-producing jet. Our previous experimental study (Mahulkar and Arakeri, (2024)) compared the flow fields of the clapping body in two cases: free-moving (dynamic) and forward-constrained (stationary). The experiments revealed significant differences in body motion and flow structures. This numerical study further investigates these differences using plate motion data from the experiments. Our computations show that, in dynamic cases, interplate cavity pressure is lower than in stationary cases. A basic unsteady Bernoulli analysis explains that forward acceleration reduces interplate pressure. Furthermore, stationary cases exhibit distinct vortex dynamics, with starting vortex tubes forming at the plate edges and reconnecting with stopping vortex tubes to form triangular vortex loops in the rear wake, along with two sideways-oriented ringlets. In dynamic cases, the starting vortex tubes slide backward and reconnect with bound-vorticity threads shed from the outer surface of the plates, forming elliptical loops that reconnect circumferentially. Referring to Sullivan *et al.* (2008), we quantify the energy deficit in isolated axisymmetric vortex rings using separate simulations and propose a model for the potential energy in the vortex core at the formation time. Using this model, we show that the total wake energy (kinetic + potential) equals the initial slug energy for the vortex ring, and in clapping, it equals the work done on the fluid by the pressure torque on the plates. [250 words]

Key words: Propulsion, swimming/flying, vortex dynamics

1. Introduction

In aquatic habitats, animals such as squid and jellyfish commonly use pulse jet propulsion. Interestingly, a review article by Gemmell *et al.* (2021) highlights numerous other marine invertebrates that utilize this propulsion method, as well as their swimming performances. In recent years, there has been a notable increase in flow dynamics research related to pulse jet propulsion, as reflected in the development of several aquatic robots powered by pulse jets. Examples include Robosquid (Nichols, Moslemi and Krueger (2008)), CALAMAR-E (Krieg and Mohseni (2008)), flexible robots with eight radial arms (Bujard, Giorgio-Serchi and Weymouth (2021)), and biohybrid robots (Xu and Dabiri (2020)). These robots are primarily inspired by the jet production mechanism observed in jellyfish and squid. In jellyfish, the contraction of the umbrella cavity produces a starting vortex ring during thrust-producing phases (Dabiri *et al.* (2005), (2006)). Squid operate similarly, though their wake patterns may vary, showing

† Email address for correspondence: suyogm@iisc.ac.in

either isolated vortex rings or rings with a trailing jet (Bartol *et al.* (2009), (2016)). Pulse jet production is also observed in butterflies, particularly during the clapping phase of wing motion (Brodsky (1991) and Johansson and Henningsson (2021)). This clapping motion offers an alternate, mechanically simple method for producing pulse jets. D. Kim *et al.* (2013) conducted the first controlled study on two clapping plates submerged in an quiescent fluid to investigate thrust generation and associated flow fields. Upon comparing clapping and flapping, Martin *et al.* (2017) observed that while clapping produces greater thrust, flapping is a more efficient mode of propulsion.

In the real world, aquatic animals eject a pulse jet while moving forward. To understand how body motion influences pulse jet production, we conducted an experimental study (Mahulkar and Arakeri (2023)) using a freely moving clapping body consisting of two plates hinged at one end and initially pulled apart at the other end (see figure 1). Upon actuation, the body performs a closing (or clapping) motion of the interplate cavity, generating thrust that propels it forward. Compared to forward translation, these plates performed the clapping motion much faster. Note that previous studies on pulse jet formation typically use stationary bodies (Kim *et al.* (2013), Martin *et al.* (2017), Das *et al.* (2013), (2018)). However, our subsequent study investigates whether allowing a stationary body to move freely alters flow dynamics (Mahulkar and Arakeri (2024)). In this study, we conducted experiments using the clapping body in two cases: the *Dynamic case*, where the body moves freely while performing the clapping motion, and the *Stationary case*, where forward motion is constrained but clapping motion is allowed. Surprisingly, our findings revealed significant changes in both the near-body flow field and wake evolution between the stationary and dynamic cases. An almost twofold increase in the rotation speed of the clapping plates observed in the dynamic case experiments reflects significant changes in the three-dimensional near-body flow field. Furthermore, the changes in wake evolution were partly understood from the evolution of vortices captured using two-dimensional (2-D) particle image velocimetry (PIV). The wake vortices in dynamic cases evolved as circumferentially connected vortex ringlets, similar to the vortex structure formed after a head-on collision of vortex rings (Lim *et al.* (1992)). In contrast, stationary cases showed separate ringlet formations at the back, top, and bottom sides (see figure 15 in Mahulkar and Arakeri (2024)). Although 2D PIV used in the experimental analysis quantified certain aspects of the flow field, such as the overall flow structure and the strength of starting vortices, understanding some crucial aspects requires three-dimensional data. These primarily include two aspects: first, how the evolution of the pressure field around the clapping plates is linked to their translation, which results in different angular velocities between the stationary and dynamic cases; second, how the onset of reconnection between the two vortex loops (one for each plate) differs across the cases, leading to distinct wake structures, as observed in the experiments. To investigate these aspects, we performed three-dimensional viscous computations of clapping motion. In the computations, we modeled the interplate cavity essentially using two rotating plates, with plate motion data obtained from experiments. We conducted four simulations, solving for two body depths in both stationary and dynamic cases. After introducing the computational model in the next section (§2), we present the details of the parametric space considered in this study.

We also investigate the energy budget of a wake of an isolated vortex loop without a trailing jet, as observed in both stationary and dynamic clapping cases. For an isolated vortex ring, Sullivan *et al.* (2008) reported an interesting observation regarding momentum and energy conservation in their study, where an impulsively moving piston discharges water through a cylindrical gun to form a thin vortex ring. They found that the momentum of a fully developed vortex bubble is nearly the same as the momentum of the fluid slug discharged into the domain, but the kinetic energy in the bubble is less than the kinetic energy of the slug. They proposed a hypothesis for this energy deficit, suggesting it is potential energy invested in the formation of the vortex structure. We explore this hypothesis numerically using a separate set of simulations on axisymmetric viscous vortex ring formation. In these simulations, our interest lies in quantifying the potential energy

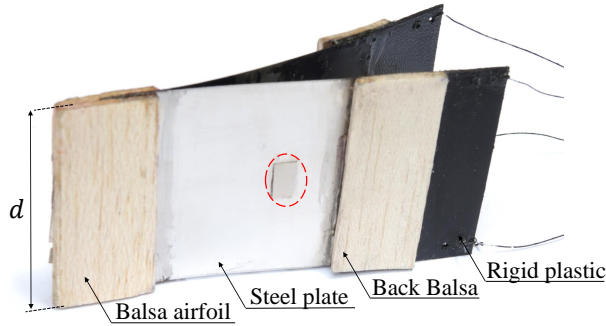


Figure 1: A perspective view of the clapping body showing both clapping plates glued together at the front. Each plate consists of a steel plate with a balsa airfoil on the front side and a rigid plastic plate with a balsa piece on the backside. The dimensions of the components are as follows: steel plate - 40 mm length, 0.14 mm thickness; rigid plastic plate - 30 mm length, 0.7 mm thickness; back balsa piece - 18 mm length, 2 mm thickness; front balsa airfoil - 19 mm chord length, 2 mm thickness. A small steel mass, marked by a red circle, is used for fine adjustment of the buoyancy of the body when it is submerged in water. A fishing thread with a diameter of 0.25 mm is tied at the top and bottom corners of the trailing edges to form a threaded loop, part of which is visible in this image. The total body length, L , is 89 mm, with a depth, d , of 45 mm.

(or deficit energy) and developing a model for it that can be applicable to both axisymmetric vortex rings and the irregular vortex loops observed in the clapping wake. We study a total of six cases of axisymmetric rings, which consist of three stroke-to-diameter ratios and two different jet injection velocity programs, with further details provided in §4.3.1.

This paper is organized as follows: the computational model for the clapping body is discussed in §2, and the simulation results are compared with the experiments in §3. The main findings of this study are organized into the following sections: the flow field near the clapping body (§4.1), the flow field in the wake zone of the clapping body (§4.2), and the wake energy budget (§4.3). After introducing the energy deficit concept in §4.3, the wake energy analysis for an axisymmetric vortex ring and the clapping body is discussed in §4.3.1 and §4.3.2, respectively. The concluding remarks are presented in §5.

2. Computational modeling

In our previous experimental study on pulse jet propulsion (Mahulkar and Arakeri, (2023)), we developed a clapping body consisting of two steel plates hinged together at one end and pulled apart at the other. When allowed, both plates come close and thereby eject the fluid from the interplate cavity, resulting in a thrust-producing jet. The experiments were performed with the body submerged to a depth of 15 cm in a quiescent water tank with dimensions of 80 cm × 80 cm and a height of 30 cm. The perspective and top views of the body are shown in figures 1 and 2(a), respectively. These figures reveal the design details of each plate: a balsa piece with an aerofoil shape is attached to the leading edge, while at the trailing end, a rigid plastic piece is glued, and a rectangular cross-section balsa piece is attached on top of it. In this design, the steel plates essentially perform the clapping. However, the plastic plate and balsa pieces are used to maintain near-neutral buoyancy in the water, with their positions carefully chosen to ensure coincident

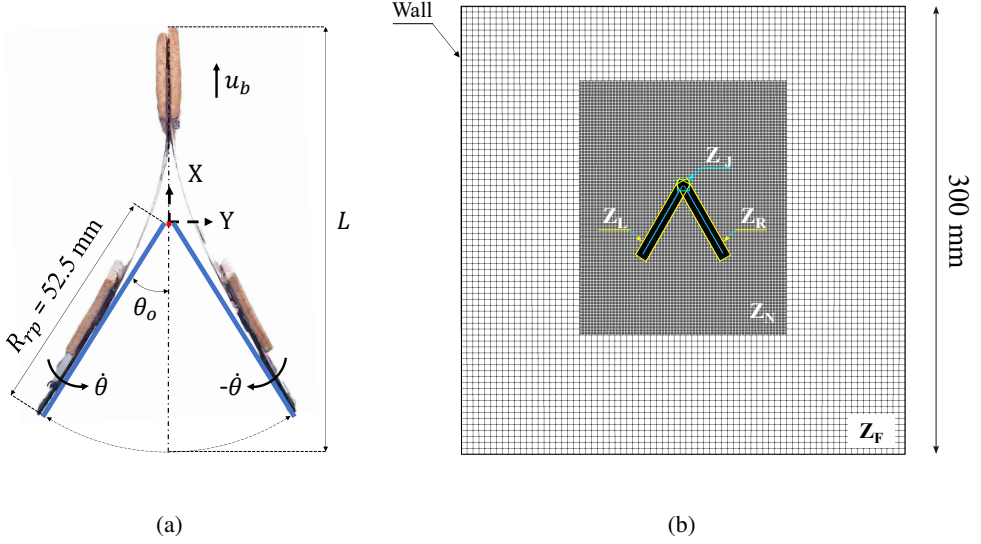


Figure 2: (a) The computational model of the clapping body consisting of two longer rigid plates (52.5 mm length, 0.7 mm thickness) in blue and a shorter interconnecting joint plate (0.7 mm length, 0.7 mm thickness) in red. The model, superimposed on the top view of the actual clapping body, shows the longer plates tangent to the rear portion of the rigid plastic in the clapping plate (see figure 1). In both stationary and dynamic cases, equal and opposite angular velocity, $\dot{\theta}$, is applied to the longer plates. Additionally, in dynamic cases, equal translational velocity, u_b , is applied to all plates. Note that the inertial coordinate system aligns with the initial position of the joint plate. (b) Top view of the 3D overset mesh domain, displaying the background mesh zone, Z_F , and two component mesh zones: one, the body-enveloping zones consisting of Z_L , Z_R , and Z_J , enveloping the left, right, and joint plates, respectively; and two, the near-body zone, Z_N . The mesh cell sizes are finest (0.35 mm) in Z_L , Z_R , and Z_J , coarsest (4 mm) in Z_F , and intermediate (1 mm) in Z_N .

mass and buoyancy centers. Further design details of the body are discussed in Mahulkar and Arakeri, (2023).

In the present study, we performed computational modeling of the closing motion of the interplate cavity using clapping plate motion data for dynamic and stationary cases, as reported in our previous experimental study (Mahulkar and Arakeri (2024)). We used three rigid plates to model the clapping motion. As shown in figure 2(a), the two longer rigid plates (blue) are tangent to the backside of the clapping plates, while a third, shorter plate (red), called the joint plate, is positioned between the two longer plates, resembling a smaller hinge. The origin of the coordinate axes in an inertial reference frame coincides with the centroid of the joint plate at the initial time, where the X and Y directions are aligned along and perpendicular to the direction of forward translation, and the Z-direction is oriented along the depth of the body. The length of both longer rigid plates, R_{rp} , is 52.5 mm with a thickness, t_{rp} , of 0.7 mm, and the length of the joint plate is the same as the thickness, t_{rp} . To simplify the modeling, we omitted the rectangular balsa piece on the plastic plate (figure 2(a)). This three-plate model encompasses most of the clapping cavity, although the portion of the clapping body ahead of the joint plate is not considered. The computations were performed for a constant initial interplate cavity angle, $2\theta_o = 60^\circ$, and a constant R_{rp} , while the depth of the body, d , was 45 mm and 89 mm. In our

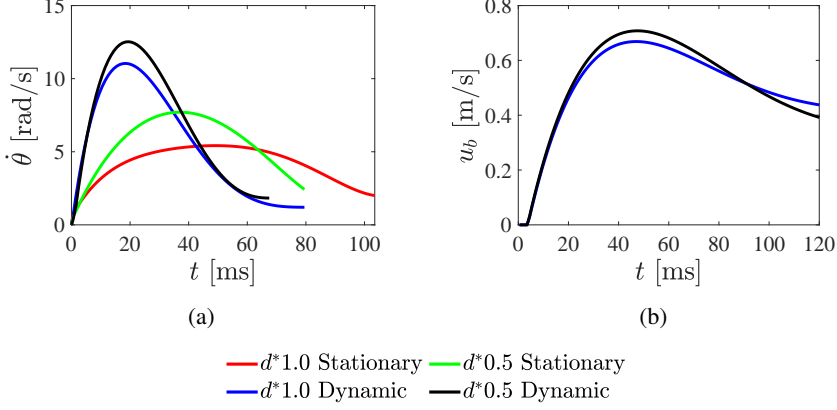


Figure 3: Experimentally obtained velocities used as input for computation: time variation of (a) the angular velocity of the clapping plate, $\dot{\theta}$; and (b) the translational velocity of the clapping body, u_b .

earlier experimental studies on the clapping body, the nondimensional depth, $d^*(= d/L)$, was obtained by normalizing the body depth by the total body length, $L = 89$ mm, as shown in figure 2. In this study, we maintained the same definition of d^* , resulting in values of d^* of 0.5 and 1.0 for $d = 45$ mm and 89 mm, respectively.

For both stationary and dynamic cases, the angular velocity of the clapping plates, $\dot{\theta}$, is extracted from the experiments using image analysis. In both cases, for d^* values of 0.5 and 1.0, $\dot{\theta}$ gradually increases with time, t , reaches a maximum, and then gradually decreases (see figure 3(a)). The data is shown up to time, t_c , which represents the time when the interplate cavity is nearly closed, with $\theta \approx 5^\circ$. Experiments show that the reduction of θ from 5 to 0 degrees occurs very slowly. During this phase, $\dot{\theta}$ decreases asymptotically until the complete closing of the clapping cavity (see figure 5(a) in Mahulkar and Arakeri, (2024)). To avoid meshing complexities associated with the complete closing of the cavity, $\dot{\theta}$ is used as a prescribed input for the rotation of the longer rigid plates over the clapping time period t_c , which covers the effective clapping duration. The t_c values listed in table 1 show faster clapping in the dynamic cases, with the maximum angular velocity, $\dot{\theta}_m$, observed in the dynamic case being nearly twice that in the stationary cases. Next, for both d^* values in the dynamic case, the evolution of the translational velocity, u_b , shown in figure 3(b), indicates that after the initial 4 ms, the body accelerates impulsively and reaches its maximum u_b toward the end of the clapping motion. Subsequently, u_b gradually decreases due to the net drag on the body. The maximum translational velocity (≈ 0.7 m/s) remains nearly constant across both d^* cases. During the clapping motion, the body covers nearly three-fourths of its length and travels approximately three body lengths before coming to a stop (at $t \approx 1$ s). The above-discussed plate kinematics are used as inputs for the computational modeling of the clapping motion. In both stationary and dynamic cases, for the rotational motion, $\dot{\theta}(t)$ and $-\dot{\theta}(t)$ are prescribed as inputs for the left and right plates (blue), respectively (see figure 2(a)). The center of rotation of each plate coincides with the corresponding edge of the joint plate (red). For the translational motion in the dynamic cases, in addition to the rotational motion, the translational velocity, u_b , along the X-direction is prescribed for all three rigid plates.

The meshing of the fluid domain around the clapping body is challenging, as it needs to withstand large displacement due to the forward motion of the body and simultaneous severe contraction due to the closing of the interplate cavity. To address this, we used the ‘Overset mesh’ technique, which can handle large mesh displacements. The overset mesh domain, shown in

Case	d^*	t_c [ms]	$\dot{\theta}_m$ [rad/s]	$t_{\dot{\theta}_m}$ [ms]	\bar{m}_B/\bar{m}_Σ [%]	\bar{m}_S/\bar{m}_Σ [%]
Stationary	0.5	79.5	7.71	36.5	39.06	60.94
	1.0	103.5	5.42	48.5	61.23	38.77
Dynamic	0.5	67.5	12.53	19.5	75.22	24.78
	1.0	79.5	11.04	18.5	88.5	11.5

Table 1: The clapping time period, t_c , maximum angular velocity, $\dot{\theta}_m$, and the time at which it becomes maximum, $t_{\dot{\theta}_m}$, are listed in columns three to five for stationary and dynamic cases of $d^* = 0.5$ and 1.0. Columns six and seven show the values for the average mass flux ejected from the backside opening of the cavity, \bar{m}_B , and the average mass flux ejected from the sideways opening of the cavity, \bar{m}_S , as a percentage of the total mass flux ejected, \bar{m}_Σ .

figure 2(b), consists of a background mesh and overlapping component meshes. The background mesh zone, Z_F , has a volume of $30 \times 30 \times 30 \text{ cm}^3$, resembling the dimensions of the water tank used in the experiments. All six surfaces of this zone are located farthest from the clapping body, and a wall boundary condition is specified on all of them. The overlapping component meshes consist of two main mesh zones: the body-enveloping zone and the near-body zone. In the body-enveloping zone, there are three separate cuboid meshes that surround the left and right clapping plates and the joint plate, denoted as Z_L , Z_R , and Z_J , respectively. In figure 2(b), the outer boundaries of Z_L and Z_R are identified by yellow rectangles, while the thick blue line shows the inner boundary that coincides with the surfaces of the rotating plates with finite depth. In the same figure, the outer and inner boundaries of Z_J are shown in cyan and red, respectively. In these component meshes, which envelop the plates, the wall boundary condition is specified on the inner boundary surfaces, while the overset boundary condition is applied to the outer boundary surfaces. Next, the second type of component mesh, the near-body zone Z_N , is a cuboid mesh zone located between the background mesh and the body-enveloping meshes, with the overset boundary condition specified on all of its surfaces. In the overset mesh, a finer resolution is maintained in the body-enveloping component meshes, while a coarser resolution is used in the background mesh, with an intermediate resolution in the near-body zone component mesh. After performing the overset mesh operation on the background and component meshes, very few orphan cells were observed along the edges of Z_J , outside the interplate cavity. Despite this, during the closing of the interplate cavity, contact between all the rigid plates modeling the cavity remained intact, as confirmed by the absence of fluid leakage from outside into the cavity. This effectively accomplished the formation of the clapping cavity using the three rigid plates.

The conservation equations for fluid mass and momentum are solved in an inertial reference frame using the commercial solver Ansys-Fluent 2020 R1. Previous studies by David *et al.* (2018) and Lee *et al.* (2012) demonstrate the solver’s reliability in resolving flow fields generated by the independent rotation and translation of a rigid plate, respectively. In the present study, the solver is used to resolve the flow field generated by the transrotation of the plates in the clapping body. For this purpose, in the 3D unsteady viscous clapping computations, the following discretization schemes are used: ‘least square cell’ for the gradient, ‘second order’ for pressure, and ‘second order upwind’ for momentum. A pressure-based coupled algorithm is used for pressure-velocity coupling, and temporal discretization is performed using the ‘first order implicit’ scheme. A time step of 0.25 ms is used for all the cases, ensuring that the Courant–Friedrichs–Lewy (CFL) value is less than 0.5. Water is used as the fluid medium, with a density of 998.2 kg/m^3 and a viscosity of 0.001 kg/m.s . A residual criterion of $1\text{E-}04$ is ensured for each time step in the clapping

computations discussed in this study. Following Fluent guidelines for post-processing the overset mesh, ‘solve’ and ‘donar’ cells are retained, while ‘receptor’, ‘dead’, and ‘orphan’ cells are filtered out. This filtering is performed in the post-processing software, ParaView.

Further, we examined grid independence for the dynamic case of $d^* = 0.5$ across three mesh configurations: ‘Coarse mesh’ (14,80,352 cells), ‘Medium mesh’ (19,98,328 cells), and ‘Fine mesh’ (39,82,656 cells). Note that all three mesh configurations consist only of hexahedral cells. For comparison across the mesh configurations, we used the fluid velocity ejected from the clapping cavity, \bar{u}_e , averaged over the opening width on the XY plane ($Z=0$). Over the clapping time period, the difference in \bar{u}_e between the coarse and fine mesh configurations remains within $\pm 13\%$ of the fine mesh value, while the difference between the medium and fine mesh configurations stays below $\pm 6\%$ of the fine mesh value. Consequently, the fine mesh configuration, as shown in figure 2(b), is selected as the finalized mesh configuration for further flow field investigations. In this configuration, a hexahedral mesh is used in all zones, with cell sizes of 4 mm in Z_F , 1 mm in Z_N , and 0.35 mm ($= 0.5 t_{rp}$) in Z_L , Z_R , and Z_J . This variation in mesh element size across the overset mesh zones is due to the limitations of our computational resources. Further, the flow field obtained from the fine mesh configuration is compared with the experimentally observed flow field in the next section.

In dynamic cases for both d^* values, simulations are conducted over a period of 132 ms. During this time, the body completes its clapping motion and travels approximately three-quarters of its length. To accommodate further displacement, a larger mesh volume in the near-body zone, Z_N , is required, but this exceeds computational resource limitations. However, this constraint does not apply to stationary cases, where the body does not translate. Therefore, while maintaining the same mesh count as in the dynamic simulations, the simulation time for both d^* values in stationary cases is extended to 250 ms. Apart from the simulation time, the body position, particularly the hinge (or joint link) location, also differs between the cases. In the dynamic case, the hinge is placed near the centroid region of Z_N (figure 2(b)), whereas in the stationary case, it is shifted closer to the upstream boundary of Z_N (not shown). This adjustment in the stationary case effectively allocates a larger fine-mesh volume in the wake zone, which is necessary for studying wake evolution over a longer duration compared to the dynamic case. Note that, to prevent complete intersection of the body-enveloping mesh zones, Z_L and Z_R , during cavity closure, clapping is performed only until θ reaches approximately 5° in both stationary and dynamic cases.

3. Comparison between experiments and computations

In the experiments, we used 2D-PIV independently on the XY plane ($Z=0$) and the XZ plane ($Y=0$) to measure the transient flow field developed due to the closing of the interplate cavity. The XY plane data, recorded from the top view of the body, captured the evolution of the flow field during the clapping motion. The XZ plane data, recorded from the side view, captured the sideways flow in the $\pm Z$ directions. Note that on the XZ plane, the flow field within the interplate cavity became invisible due to shadowing by the plate. In both PIV analyses, the interrogation window size was 24×24 pixel², where 1 pixel ≈ 0.3 mm, and data were recorded at 1000 FPS. Further details on the PIV setup can be found in Mahulkar and Arakeri, (2024). In this section, we first discuss the flow field evolution during the closing of the interplate cavity using PIV data on the XY plane and compare it with computational data. This is followed by a comparison of the flow fields on the XZ plane from both PIV and computational data after the clapping motion has ended.

The PIV field in the stationary case for $d^* = 0.5$, at the initial phase of the clapping motion ($t = 0.25t_c$), shows the fluid jet begins to eject from the opening of the cavity (see figure 4(a)). The flow field in this figure is colored by the Z-component of vorticity, ω_z , with values higher

than 5% of its maximum value. Red-blue patches identify the onset of starting vortices formation at the trailing edge of the plate, and green color represents regions of near-zero vorticity. The black line shows the tangent to the rear part of the plate, extrapolated to the hinge point, and the gray region at the backside of the plate indicates the shadow region in the PIV. In the end phase of clapping, at $t = 0.75t_c$, the PIV field in figure 4(c) shows a higher jet velocity at the cavity opening, and prominent starting vortices which lag behind the rotating plates. Eventually, both starting vortices come closer due to self-induced velocity (not shown). Note that the pair of starting vortices shown in the XY plane represents a cross-section of the 3D vortex loop enveloping the plate edges, and the evolution of the 3D wake vortices is discussed separately in §4.2. For comparison, we include the computationally obtained flow field on the XY plane ($Z = 0$) at the same time as the PIV field. The computational flow field shown in figure 4(b) at the initial clapping phase ($t = 0.25t_c$) and figure 4(d) at the end phase ($t = 0.75t_c$) closely matches the PIV vector field, except for the higher vorticity of the starting vortices in the computation, as indicated by darker red and blue colors. The reasoning behind this discrepancy is discussed later in this section. Additionally, the computational flow field captures the flow behind the rotating plate, which was shadowed in the PIV. After the clapping motion ends, in the stationary case, the PIV flow field on the XZ plane ($Y = 0$) shows a significant jet from the sideways (top and bottom side) openings of the interplate cavity, see figure 22(d). In the figure, the oppositely oriented sideways jet, ejected during clapping, is shown in red and blue, and the gray rectangle shows the shadow region. Note that the flow field on the XZ plane is colored by the Z-component of velocity, u_z . For comparison, the computational flow field on the XZ plane shown in figure 22(b), plotted for the same time instance as the PIV, also captures significant sideways flow and exhibits overall close similarity with the PIV field. The XZ flow field, in both experiment and computation, is plotted after the end of clapping motion, specifically at times when the kinetic energy in the wake at the backside reaches maximum values. We provide further discussion on this flow field in the wake energy section (§4.3.2), using the understanding of how 3D wake vortices induce the flow field, which is discussed later in this paper. Further, the flow field comparison between the experiment and computation for $d^* = 1.0$ in the stationary case largely follows the same description as discussed above for $d^* = 0.5$.

For the dynamic case of $d^* = 0.5$, as the body begins forward translation after 4 ms (figure 3(b)), part of the fluid in the interplate cavity moves in the direction of the body, while the remaining fluid is ejected in the opposite direction. This is shown in the PIV field plotted in figure 4(e) for the initial phase of clapping ($t = 0.25t_c$). Red and blue patches in the figure represent the starting vortices formed by the rotation of the plate, which occurs simultaneously with the translation. In the end phase of clapping ($t = 0.75t_c$), as the body continues to move forward, the starting vortices detach from the body and lag behind it, see figure 4(g). For comparison, we include the computational flow fields for $d^* = 0.5$ at the initial phase of clapping (figure 4(f)) and at the end phase of clapping (figure 4(h)). These flow fields exhibit a close match with the experimentally obtained flow fields. The computational flow field also captures the vorticity shed from the outer surfaces of the translating plates, visible between the trailing edges and the starting vortices (figure 4(h)), which was not captured in the PIV field for the chosen interrogation window. Further, the XZ flow field in the dynamic case, plotted for the post-clapping phase, shows a close match between the computational data and the experimental data, as shown in figures 22(a) and (c), respectively. Similar to the stationary case, this flow field is described in more detail in the wake energy section (§4.3.2). Notably, the XZ flow field in the dynamic case shows almost negligible sideways flow compared to the stationary case, as observed in both the computational and experimental flow fields. The comparison discussed above between experimental and computational flow fields for $d^* = 0.5$ is also largely valid for $d^* = 1.0$.

In both stationary and dynamic cases, the starting vortices in the experimentally obtained flow field exhibit lower vorticity. This is primarily due to the 2mm thick balsa piece attached to the

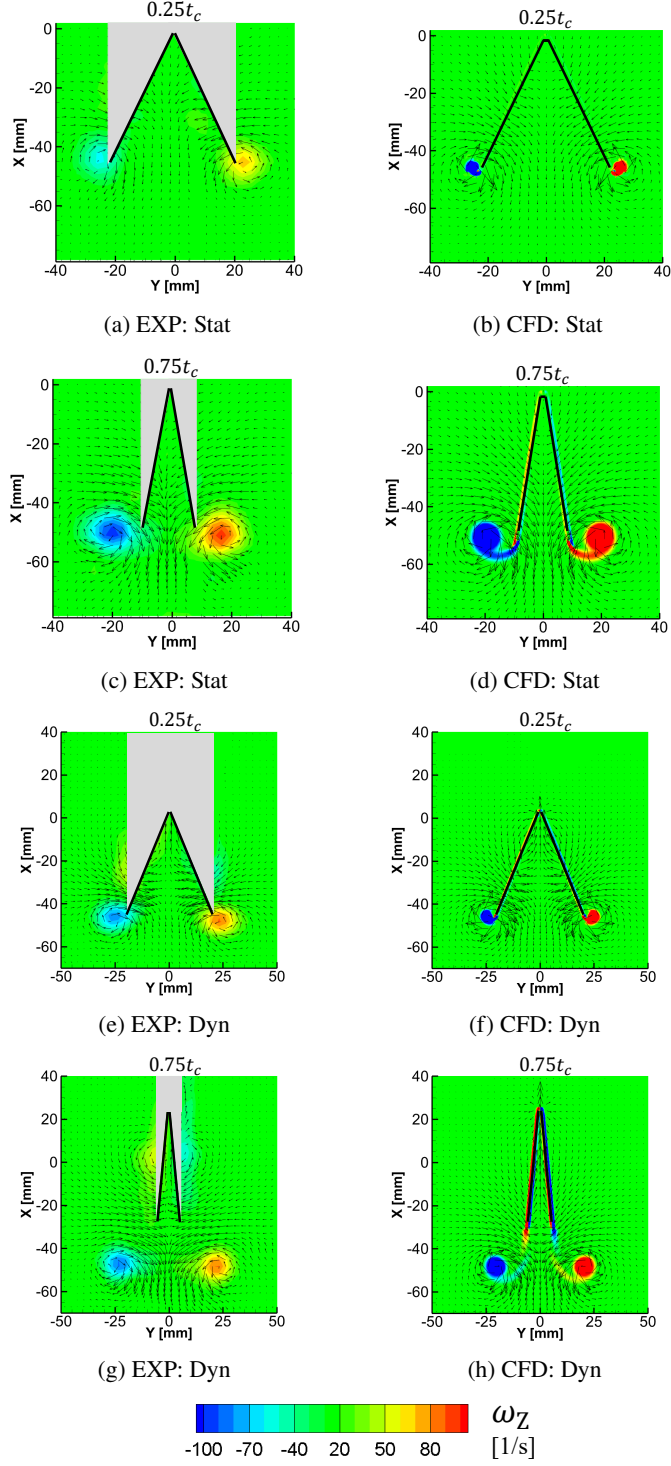


Figure 4: Comparison of experimental (EXP) and computational (CFD) flow fields for stationary (Stat) and dynamic (Dyn) cases of $d^* = 0.5$. The flow fields, plotted at $t = 0.25t_c$ (a, b, e, and f) and $t = 0.75t_c$ (c, d, g, and h), show velocity vectors and the Z-component of vorticity, ω_Z , on the XY plane at $Z = 0$.

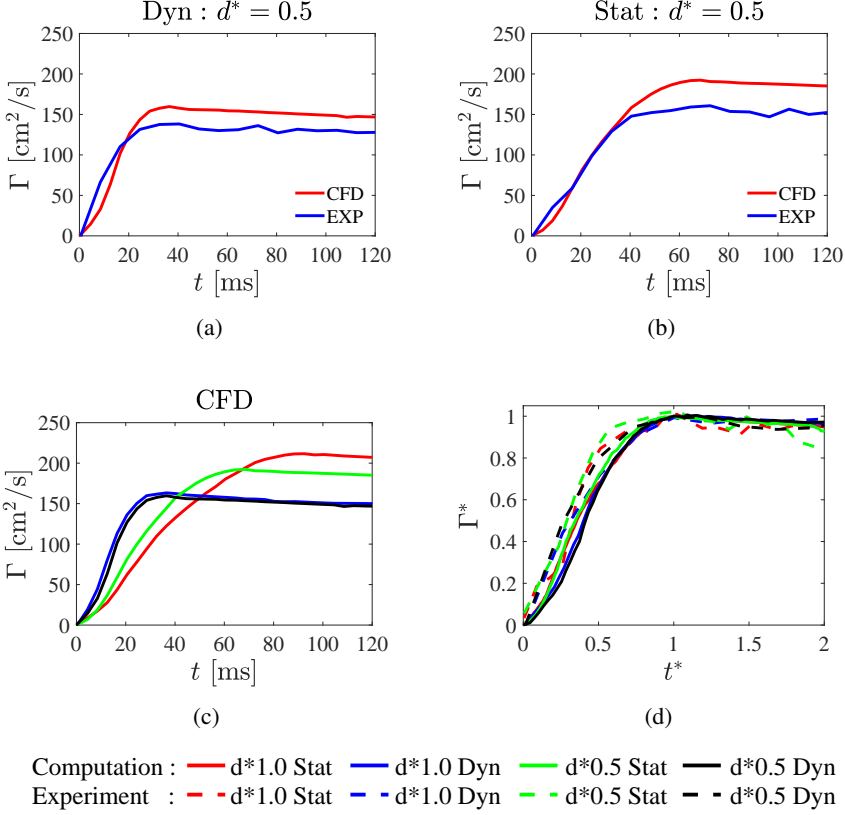


Figure 5: Evolution of starting vortex circulation, Γ , with time, t : (a) and (b) compare the computationally obtained values (CFD), shown in red, with the experimentally obtained values (EXP), shown in blue, for the dynamic (Dyn) and stationary (Stat) case of $d^* = 0.5$; (c) compares the evolution of Γ obtained from computations for stationary and dynamic cases for $d^* = 0.5$ and $d^* = 1.0$; (d) shows a plot of nondimensional circulation, $\Gamma^* (= \Gamma/\Gamma_m)$, versus nondimensional time, $t^* (= t/t_{\Gamma_m})$. Here, the maximum circulation, Γ_m , and the time to reach maximum circulation, t_{Γ_m} , are used to normalize Γ and t , respectively. Data from experiments and computations for both d^* values in stationary and dynamic cases are compared, with the corresponding legends provided below the plot.

backside of each plate in the clapping body used in the experiments (figure 2(a)). The fluid flow downstream of the plate, especially near the corner of the balsa piece, locally separates, creating larger velocity gradients. Compared to the flat plate geometry used in the computations, the 2mm projection of the balsa piece enhances vorticity shedding from the backside of the plate, which is partially visible in the PIV field near the outer surface of the plates, as seen in figure 4(g). This vorticity is oppositely oriented and weaker than the vorticity shed from the front side of the plate, which faces the interplate cavity. Near the trailing edge, the interaction of oppositely shed vorticities from the back and front sides reduces the front-side vorticity, which eventually rolls up into the starting vortex. This reduction is negligible in the flat plate geometry used in the computation. Consequently, the starting vortices observed in the computations exhibit higher vorticity values, and this difference in vorticities is further quantified using the circulation, as discussed below.

The rotation of the plate in an initially quiescent fluid domain initiates the formation of the

Case	d^*	$\Gamma_m [\text{cm}^2/\text{s}]$		$t_{\Gamma_m} [\text{ms}]$	
		CFD	EXP	CFD	EXP
Stationary	0.5	192.3	156.9	68.5	70.5
	1.0	211.4	196.2	88.5	94.5
Dynamic	0.5	158.7	138.8	33.5	33.5
	1.0	163.1	138.9	31.5	32.5

Table 2: Maximum circulation in starting vortices, Γ_m , obtained from computational (CFD) and experimental (EXP) data are listed in columns 3 and 4, respectively, for stationary and dynamic cases for $d^* = 1.0$ and $d^* = 0.5$. Columns 5 and 6 list the corresponding times, t_{Γ_m} , when the circulation reached its maximum value.

starting vortex. As the rotation continues, vorticity feeding increases its strength, reaching a maximum toward the end of the clapping motion. The strength of the vortex is quantified by the circulation $\Gamma (= \int \omega_Z dA_{cr})$, calculated using the Z-component of vorticity, ω_Z , in the XY plane ($Z=0$) over the vortex core area, A_{cr} . The vortex core is identified using the vorticity criterion: $\omega_Z \geq 5\% \omega_{Z|\max}$. The evolution of Γ for $d^* = 0.5$ in both dynamic and stationary cases shows an initial gradual increase, reaching a maximum steady value, as shown in figures 5(a, b). A similar evolution of Γ is observed for $d^* = 1.0$. In these figures, the experimental values of Γ are slightly lower than the computational values. This difference is attributed to the balsa piece at the backside of the rotating plate in the experiments. As discussed above, the oppositely oriented vorticity shed from this piece partially cancels the vorticity in the starting vortex, reducing its circulation. Interestingly, in both experiments and computations, the maximum steady circulation value, Γ_m , is higher for stationary cases and increases with d^* , while in dynamic cases, it remains lower and relatively constant for both d^* values (see figure 5(c) and table 2). The lower circulation in dynamic cases occurs because the starting vortices detach earlier from the forward-moving plates (figures 4(g) and (h)), allowing vorticity feeding into them for a shorter duration. In contrast, in stationary cases, starting vortices remain close to the plates, enabling vorticity feeding for a longer time, as reflected in the larger circulation values. Further, the increase in Γ_m with d^* in stationary bodies is primarily due to reduced sideways flows as body height (or d^*) increases. This reduction in sideways flow leads to higher flow velocity in the wake behind the body, reflecting an increase in circulation with d^* . In contrast, in the dynamic cases, negligible sideways flow results in nearly constant Γ_m over d^* variations. These aspects were discussed in detail in our previous experimental study (Mahulkar and Arakeri, (2024)), where we explained the variation in Γ_m with d^* using integral mass conservation over the interplate volume and an approximate slug-circulation model. Furthermore, the time, t_{Γ_m} , at which the starting vortex reaches its maximum value, shows a very close match between computational and experimental data (see table 2). Its variation with d^* follows the same trend as that of Γ_m . Further, nondimensional circulation, $\Gamma^* (= \Gamma/\Gamma_m)$, when plotted against nondimensional time, $t^* (= t/t_{\Gamma_m})$, shows a collapse of curves for dynamic and stationary cases extracted from both computational and experimental data for both d^* values, see figure 5(d). This shows that, despite the variation in the maximum circulation after constraining forward motion, the overall nature of circulation evolution remains the same across the parametric space. Thus, in both stationary and dynamic cases, for both d^* values, the close agreement between the computational and experimental flow fields, along with the similar evolution of starting vortex circulation (with magnitudes within the same range), validates the computation.

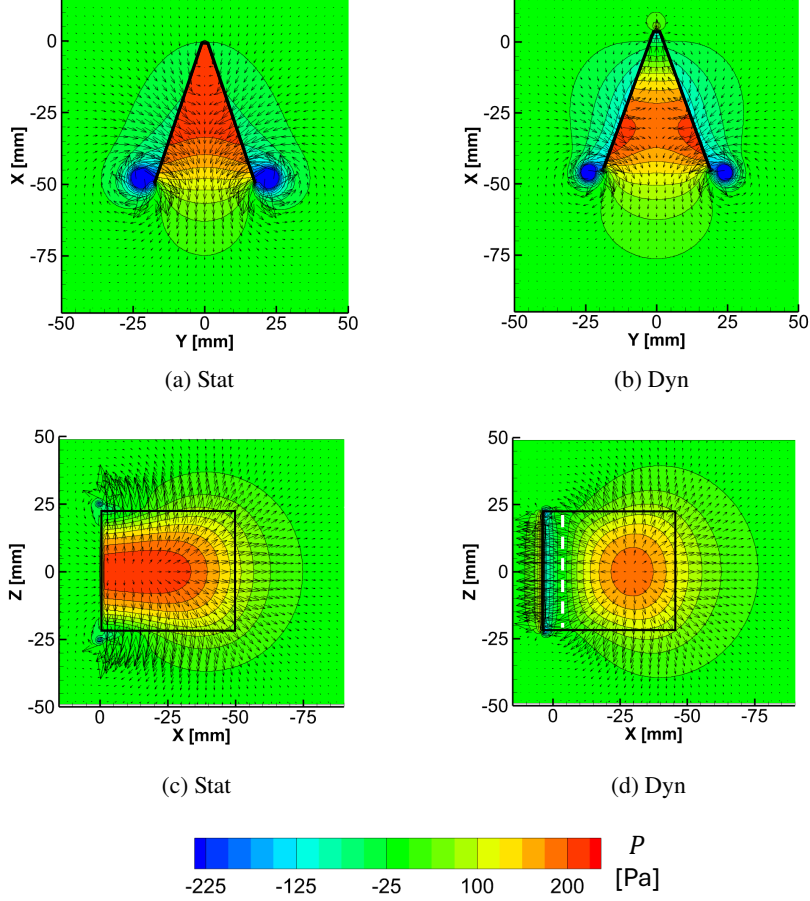


Figure 6: Static pressure (gauge) field and velocity vectors at the time $t_{\dot{\theta}m}$, when the angular velocity of the plate reaches its maximum value (table 1). The flow field is plotted on the XY plane ($Z=0$) for (a) the stationary case (Stat) and (b) the dynamic case (Dyn) for $d^* = 0.5$, and on the XZ plane ($Y=0$) for (c) the stationary case and (d) the dynamic case for the same d^* value. In (a) and (b), the top view of the clapping body is represented by two black lines, while in (c) and (d), the side view projection of the clapping plate is shown as a rectangle. In (d), the white dashed line marks the transition zone, where the pressure is negative (blue) on the left side and positive (red) on the right side. This zone is observed only in the dynamic case.

4. Results and discussion

4.1. Flow around the body

In this section, we examine the flow field around the clapping body, focusing on how the pressure distribution and the ejected flux from the interplate cavity openings change when the stationary clapping body is allowed to move freely.

4.1.1. Pressure distribution

In this section, we first discuss the pressure field generated by the stationary clapping body of $d^* = 0.5$. The rotation of plates from the initial rest condition shrinks the interplate cavity. This forces the fluid available inside the cavity into a smaller space and causes the pressure inside to

rise. Meanwhile, due to inertia, the fluid on the backside of the plate lags behind its rotation. As a result, the fluid does not accelerate as quickly as the plate, and the resulting discrepancy is reflected as negative pressure on the plate's backside. The static pressure (gauge) distribution on the XY plane ($Z=0$), as shown in figure 6(a), shows higher pressure than ambient (referred to as positive pressure) inside the cavity (red) and lower pressure (referred to as negative pressure) on the backside of the plate (blue). The rotation of both plates forms starting vortices near the trailing edge, which show low-pressure values in their core regions. Next, we discuss the pressure variation in the depth direction, which primarily arises due to the finite aspect ratio of the body. The maximum pressure region is located around the mid-depth of the plate, spanning approximately two-thirds of its length from the leading (hinge) side. The pressure gradually decreases toward the cavity openings, as shown in the XZ-plane flow field in figure 6(c). This flow field shows that the cavity expels fluid from the top, bottom, and backside of the body, while the flow restriction on the front side builds up the pressure. At the top and bottom corners of the front side, small negative pressure regions indicate the pressure in the cross-section of the starting vortex tube, which is present along the edges of both plates (see figure 11(a)). The above description explains the pressure field associated with the effective clapping phase. However, in the final phase of clapping, a *pressure crossover* is observed at time, $t_{\pm p}$, of 70 ms, when negative pressure develops inside the closing cavity and positive pressure outside (not shown). In this phase ($t \geq t_{\pm p}$), the force applied by the plate to drive the fluid diminishes considerably. Still, the fluid already in motion continues due to its inertia, creating a momentum deficit between the fluid adjacent to the plate and the surrounding flow in the cavity. This deficit gives rise to negative pressure, which remains uniform along the body depth. Meanwhile, on the outer side of the plate, the plate opposes the inertial motion of the fluid. This resistance to fluid motion leads to a buildup of pressure outside the cavity. After the end of the rotation, the pressure field around the body gradually returns to nearly ambient (zero gauge) pressure. We quantify the effect of pressure changes on the body (both plates) using the thrust coefficient metric, which is discussed later in this section. The pressure field description remains the same for the stationary body of $d^* = 1.0$, except for a slight delay in pressure crossover ($t_{\pm p} = 85$ ms), attributed to the delayed closing of the clapping motion ($t_c = 103.5$ ms, see table 1).

For the dynamic case of $d^* = 0.5$, in the first 4 ms, both clapping plates perform only the clapping motion without translation. During this time, similar to the stationary case, positive pressure develops inside the interplate cavity and negative pressure outside. After 4 ms, as the body starts its forward motion, the flow field shows surprising changes, see figure 6(b). The figure shows that in the clapping cavity, close to the hinge region, the pressure is slightly lower, whereas toward the trailing edge, positive pressure develops, in contrast to the stationary case, which shows only high pressure in the cavity. Interestingly, the pressure field observation on the XZ plane (see figure 6(d)) reveals three main transformations due to the forward motion of the body: first, it forms a pressure transition region inside the interplate cavity where the pressure is nearly ambient, identified with a white dashed line; second, the positive pressure distribution becomes nearly axisymmetric in the cavity; and third, the zone of maximum pressure (red), where the flow is nearly stagnant, shifts toward the trailing edge, whereas in the stationary case, it was near the leading edge. This axisymmetric pressure zone in the interplate cavity moves with the body. Next, similar to the stationary case, the pressure outside the cavity is negative, except at the hinge region, where stagnation causes higher pressure. Additionally, the flow field in the XZ plane also shows that sideways flow is significantly reduced due to the body's forward motion. The above discussion primarily explains the pressure field in the effective clapping phase. However, as observed in the stationary case, a pressure crossover also occurs in the dynamic case at $t_{\pm p} = 40$ ms, where the pressure inside the cavity becomes completely negative (not shown). Note that at this phase, the clapping cavity is nearly closed. Further, in contrast to the stationary case, where the pressure field eventually reaches ambient, the dynamic case exhibits a second pressure crossover around

60 ms (not shown). Here, the fluid trapped in the very narrow interplate cavity is dragged along with the purely translating body, resulting in low positive pressure inside the cavity (~ 10 Pa) and low negative pressure of similar magnitude outside, particularly toward the trailing edges. The pressure description at the hinge point remains unchanged. This second pressure crossover can be understood by noting that the inertia of the trapped fluid causes it to accelerate relative to the cavity, whose narrowing geometry contracts the flow. However, the confinement imposed by the plate restricts this acceleration, leading to a buildup of pressure. Conversely, at the trailing edges, the base of the triangular interplate cavity induces flow separation and wake formation, resulting in a localized region of negative pressure relative to ambient. In this phase, the thrust coefficient is nearly zero, as discussed below. Crucially, a second pressure crossover cannot occur if the interplate cavity fully closes. For the dynamic case of $d^* = 1.0$, this pressure field description remains the same.

As discussed above, during the effective clapping period, in both stationary and dynamic cases, the pressure on each plate is predominantly positive on the front side (facing the interplate cavity) and negative on the backside. When the pressure is integrated over the plate surface, the resulting forces on both sides act in the same direction (see force vectors near the trailing edge of the plate in schematics 8(b) and 9(b)). The X-component of this combined force contributes to thrust. The total thrust, F_T , is obtained by summing the thrust contributions from both plates. Based on this, the thrust coefficient, C_T , is defined as:

$$C_T = \frac{F_T}{0.5\rho \bar{u}_T^2 A_c}, \quad (4.1)$$

where ρ is the fluid density, $\bar{u}_T (= R_{rp} \int_0^{t_c} \dot{\theta} dt / t_c)$ is the mean tip velocity obtained from the angular velocity of the plate, and $A_c (= R_{rp} d)$ is the surface area of the plate with length R_{rp} and depth, d . Figure 7(a) shows the evolution of the thrust coefficient over the clapping time period, t_c , for both stationary and dynamic cases. In the stationary cases for $d^* = 0.5$ and 1.0 , the high initial C_T arises due to the impulsive rotation of the plate, which rapidly accelerates the surrounding fluid and generates steep, unsteady pressure gradients. These gradients induce strong local fluid accelerations, moving a significant mass of fluid (the added mass). The combined effect of rapid acceleration and significant added mass generates a strong reactive force, resulting in a high initial C_T , which then gradually decreases. In the end phase of the clapping motion, C_T becomes negative due to the pressure crossover occurring at $t_{\pm p}$. In the freely moving case, during the initial period of pure rotation ($t \leq 4$ ms), C_T reaches a high value. Subsequently, as the body begins to translate impulsively, C_T exhibits a sharp dip. This occurs because, when the body is free to move, a significant portion of the fluid's reactive force is diverted to accelerating the body. As a result, less reactive force remains with the fluid to generate thrust, leading to a sharp dip in C_T . Once translation begins, C_T gradually decreases, similar to the stationary cases, and becomes negative in the end phase of rotation due to the pressure crossover at $t_{\pm p}$. Around the time of rotation stopping, C_T returns to positive values close to zero due to a second pressure crossover associated with fluid dragging in the interplate cavity. Additionally, the time variation of C_T in the dynamic cases spans a shorter duration, primarily due to faster clapping compared to the stationary cases. Next, the variations in C_T with body depth are well captured using the mean thrust coefficient, \bar{C}_T , obtained by averaging C_T over the time t_c . Figure 7(b) shows that \bar{C}_T increases linearly with d^* in the stationary cases ($\bar{C}_T = 3.26$ for $d^* = 0.5$, and 4.94 for $d^* = 1.0$), whereas in the dynamic cases, it remains nearly constant with d^* ($\bar{C}_T = 2.07$ for $d^* = 0.5$, and 2.42 for $d^* = 1.0$). Following the definition of C_T , the pronounced variation in \bar{C}_T with d^* observed in the stationary cases suggests that F_T/d varies with d^* , since \bar{u}_T remains nearly invariant across different depths. This trend is further supported by our experimental study comparing stationary and dynamic cases (Mahulkar and Arakeri (2024)), which also shows that F_T/d depends on

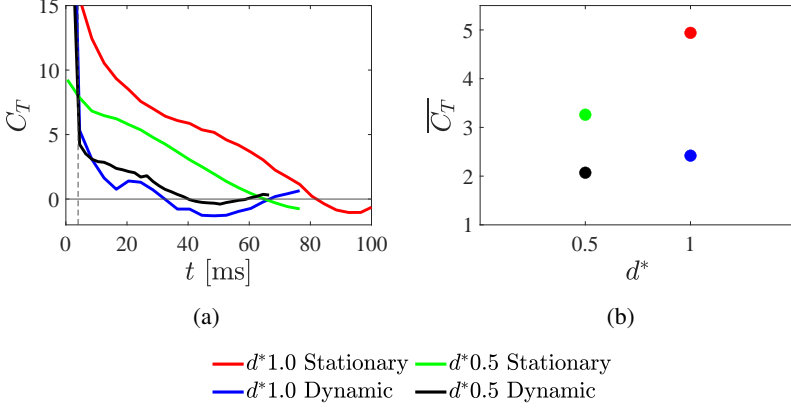


Figure 7: (a) Evolution of the thrust coefficient, C_T , with time for stationary and dynamic cases of $d^* = 0.5$ and 1.0 . The vertical dashed line indicates the time domain up to 4 ms, prior to the onset of translation in the dynamic cases. (b) Plot of the mean thrust coefficient, $\overline{C_T}$, versus d^* .

d^* only in the stationary cases. To explain this behavior, an integral momentum conservation analysis over the interplate volume was carried out in the experimental study. It revealed that F_T/d is inversely related to the proportion of sideways-ejected flow. As body depth increases, this sideways flux decreases, redirecting a greater portion of momentum along the X-direction. Consequently, both F_T/d and $\overline{C_T}$ increase with body depth (or d^*) in the stationary cases. In contrast, in the dynamic case, the effects of sideways flow are negligible, which is reflected in the nearly constant values of $\overline{C_T}$ with d^* . Further, the variations in sideways flow, expressed in terms of mass flux, are discussed in detail in the next section (§4.1.2). In the same experimental study, $\overline{C_T}$ was also estimated approximately as the ratio of wake vortex impulse to the clapping time period. These experimentally obtained values of $\overline{C_T}$ follow the same trend with d^* as observed in the present computational results, although their magnitudes are nearly half: the experimental C_T values for the stationary cases are 1.96 for $d^* = 0.5$ and 2.89 for $d^* = 1.0$; for the dynamic cases, the corresponding values are 1.15 for $d^* = 0.5$ and 1.12 for $d^* = 1.0$. This underestimation likely results from modeling the clapping wake as a vortex ring. While the actual wake structure is more complex (see §4.2), modeling choice was necessary to estimate the three-dimensional wake momentum from the two-dimensional PIV data available in the mid-depth plane.

We now perform a simple analytical investigation to understand the relationship between the clapping (or rotational) motion of the plates and the pressure field that develops across them, which differs between the stationary and dynamic cases. This analysis focuses on the starting phase of the clapping motion, where viscous effects are negligible. Additionally, for the simplification of the analysis, the pressure variation in the depth direction has been ignored. We begin by assuming a mean positive gauge pressure, $+P_f$, averaged over the front surface of the plate facing the interplate cavity, and a mean negative gauge pressure, $-P_b$, on the backside of the plate. These assumptions are consistent with the gauge pressure field observations shown in figures 6(a, b). The front-side pressure, $+P_f$, exerts a force F_{pf} directed into the plate, while the backside pressure, $-P_b$, exerts a force F_{pb} directed away from it (see figures 8(b) and 9(b)). These co-oriented forces indicate that the net pressure on each plate, P_{f+b} , computed by normalizing the total force ($F_{pf} + F_{pb}$) by the plate area, is simply the sum of the magnitudes of the gauge pressures acting on both sides:

$$P_{f+b} = P_f + P_b. \quad (4.2)$$

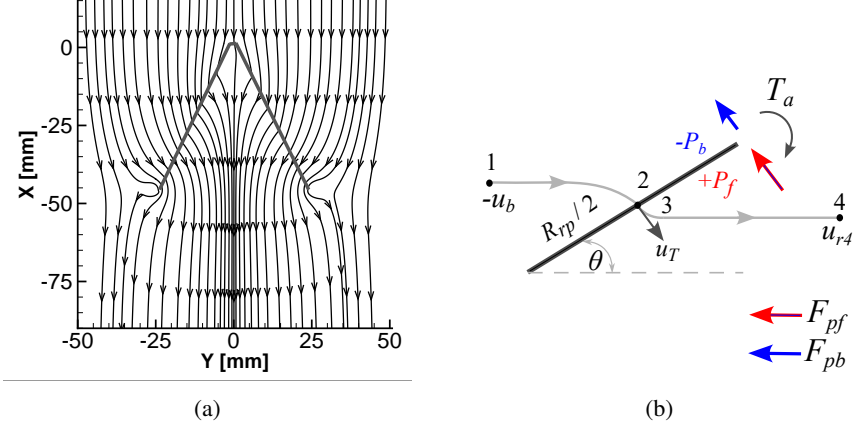


Figure 8: (a) Streamline plot on the XY plane ($Z = 0$) in the reference frame moving with the body for $d^* = 0.5$ at the initial time ($t = 10$ ms), where thick gray lines indicate the body position. (b) Schematic of the streamlines at the mid-radius of the plate (gray), oriented at a semi-clapping angle, θ . These streamlines are used to estimate the pressures on the plate's back side, $-P_b$, and front side, $+P_f$, by applying the unsteady Bernoulli equation in a non-inertial frame between points 1–2 and 3–4, respectively. The resulting pressure forces on the back side, F_{pb} , and front side, F_{pf} , due to $-P_b$ and $+P_f$, respectively, act in the same direction, generating a torque that opposes the applied spring torque, T_a , on the plate.

Interestingly, this expression shows that it is the sum of the pressure magnitudes across the plate surfaces, not the difference as commonly assumed, that governs the rotational motion. Next, we apply the unsteady Bernoulli equation in a non-inertial frame to derive expressions for P_f and P_b , starting with the dynamic case. Here, the streamline near the mid-radius region of the plate is selected for the Bernoulli analysis. The rationale for this selection can be seen from the streamline plot shown in figure 8(a), which presents streamlines in the moving reference frame at the onset of translation of the body ($t = 10$ ms). The plot reveals jet-like flow structures emerging at the cavity opening, and curved streamlines near the trailing edge indicating the presence of starting vortices. Notably, the streamline near the mid-radius on the front side of the plate, being relatively unaffected by the starting vortices, exhibits a simpler geometry, making it a suitable location for applying the Bernoulli equation. The schematic of this streamline is provided separately in figure 8(b), showing that points 1 and 2 lie on the streamline at the backside of the plate, while points 3 and 4 lie on the streamline at the front side of the plate. The unsteady Bernoulli equation in the accelerating reference frame, applied between points 1 and 2, is

$$\int_1^2 \frac{\partial \mathbf{u}_r}{\partial t} \cdot ds + \int_1^2 \mathbf{a}_F \cdot ds + \frac{P_2}{\rho} + \frac{u_{r2}^2}{2} = \frac{P_1}{\rho} + \frac{u_{r1}^2}{2}, \quad (4.3)$$

where \mathbf{u}_r is the fluid velocity relative to the translating body, ds is a differential segment along the streamline, \mathbf{a}_F is the acceleration of the reference frame, and the pressures and magnitudes of relative velocity at points 1 and 2 are denoted by P_1, u_{r1} and P_2, u_{r2} , respectively. For the derivation of this equation, see Appendix A. The first term on the LHS of (4.3), the *unsteady term*, requires variation in fluid acceleration along the streamline, which is difficult to determine. To address this, we use a scaling approach, assuming two scales: first, the characteristic scale for fluid acceleration is taken to be the tangential acceleration of the plate at point 2, given as $R_{rp}\ddot{\theta}/2$; second, the length scale of the streamline is taken as the plate radius, R_{rp} , since the flow field variations are largely captured within this length. Substituting these scales, we

obtain the scaling expression for the unsteady term as $\int_1^2 \partial \mathbf{u}_r / \partial t \cdot d\mathbf{s} \sim R_{rp}^2 \ddot{\theta} / 2$. We now solve for the second term on the LHS of (4.3), the *accelerated-frame term*, where the reference frame accelerates with the body acceleration, \dot{u}_b , in the direction opposite to the streamline. Substituting R_{rp} as the length scale in this term gives $\int_1^2 \mathbf{a}_F \cdot d\mathbf{s} \sim -\dot{u}_b R_{rp}$. With the scales for both the unsteady and accelerated-frame terms established, the remaining terms can be evaluated using the pressure–velocity description at points 1 and 2. At the beginning of translation of the body, at point 1, the pressure is assumed to be ambient ($P_1 \approx 0$), and the velocity is $u_{r1} \approx -u_b$ since the fluid is nearly quiescent in the lab reference frame. At point 2, the pressure is $P_2 = -P_b$, and the velocity can be assumed to be the plate tip velocity, u_T ($u_{r2} \approx u_T (= R_{rp} \dot{\theta} / 2)$). Substituting these values into (4.3), we obtain an expression for the pressure on the backside of the plate in the dynamic case:

$$P_{b|D} \sim \rho \left(\frac{R_{rp}^2}{2} \ddot{\theta} - \dot{u}_b R_{rp} + \frac{u_T^2}{2} - \frac{u_b^2}{2} \right). \quad (4.4)$$

Similarly, an expression for P_f can be obtained by applying the Bernoulli equation between points 3 and 4 as shown in figure 8(b). Before deriving P_f , we first obtain an expression for the mean fluid velocity ejected relative to the moving body, u_{re} , using integral mass conservation applied to the 2D triangular interplate cavity. The geometric description of the cavity is as follows: the slant length equals the plate radius, R_{rp} ; the base of the cavity, representing the opening width, is $w = 2R_{rp} \sin \theta$; and the apex angle equals the semi-clapping angle, 2θ . The mass conservation equation for this cavity is given as:

$$-\rho \dot{A}_V + \rho u_{re} w = 0, \quad (4.5)$$

where the first term on the LHS represents the rate of contraction of the interplate cavity area, $\dot{A}_V (= \dot{R}_{rp}^2 \sin \theta \cos \theta)$, while the second term represents the mass flux ejected per unit depth through the cavity opening, with u_{re} assumed uniform over w . Using small-angle approximations, the above equation simplifies to

$$u_{re} = \frac{R_{rp} \dot{\theta}}{2\theta}. \quad (4.6)$$

We now apply the Bernoulli equation between points 3 and 4, where the pressure at point 3 is $P_3 = +P_f$, and the pressure at point 4 is assumed to be ambient, $P_4 \approx 0$. The velocities at these points are taken as $u_3 \approx u_T$ and $u_4 = u_{re}$, respectively. Using the previously derived scaling estimates for the unsteady and accelerated-frame terms, we obtain the pressure on the front side of the plate in the dynamic case:

$$P_{f|D} \sim \rho \left(\frac{R_{rp}^2}{2} \ddot{\theta} - \dot{u}_b R_{rp} + \frac{u_{re}^2}{2} - \frac{u_T^2}{2} \right). \quad (4.7)$$

At the onset of translation, both angular and linear velocities of the plate are negligible: $u_T \approx 0$, $u_{re} \approx 0$, and $u_b \approx 0$. Under these assumptions, substituting (4.4) and (4.7) into (4.2) gives an approximate expression for the mean net pressure across the plate in the dynamic case:

$$P_{f+b|D} \sim 2\rho R_{rp} \left(\frac{R_{rp}}{2} \ddot{\theta} - \dot{u}_b \right). \quad (4.8)$$

Similarly, the mean pressure across the plate in the stationary case, $P_{f+b|S}$, is obtained using the unsteady Bernoulli equation in the laboratory reference frame. As in the dynamic case, we select the streamline at the mid-radius of the plate, where the influence of the stronger starting vortices is minimal. This selection is supported by the streamline plot at the onset of plate rotation ($t = 10$ ms), shown in figure 9(a), which additionally reveals a suction streamline on the backside

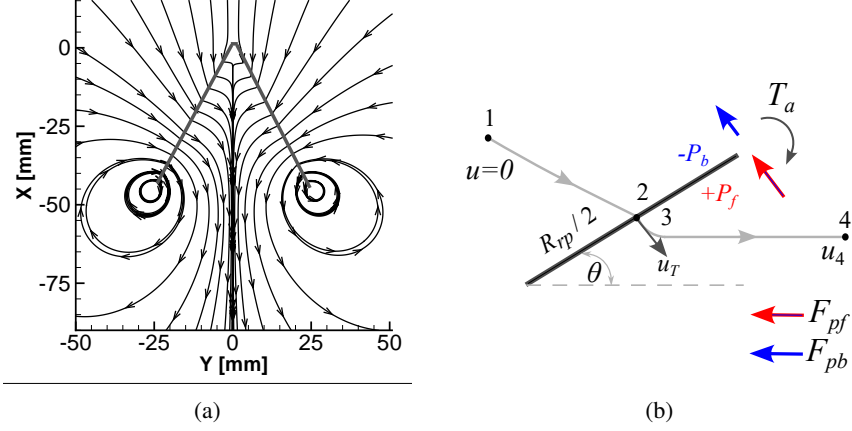


Figure 9: (a) Streamlines in the lab reference frame at the initial time ($t = 10$ ms) on the XY plane ($Z = 0$) for the stationary case of $d^* = 0.5$. (b) Schematic of the streamlines at the mid-radius of the plate, used for an approximate estimation of pressures on the plate. This figure follows the same description as given for figure 8(b).

of the plate, a jet-like structure near the cavity opening, and curved streamlines near the trailing edges of both plates that indicate the presence of starting vortices. We now apply the unsteady Bernoulli equation between points 1 and 2, as shown in figure 9(b), and substitute the scaling for the unsteady term, as derived in the dynamic case. This gives an expression for the pressure on the backside of the plate as:

$$P_{b|S} \sim \rho \left(\frac{R_{rp}^2}{2} \ddot{\theta} + \frac{u_T^2}{2} \right), \quad (4.9)$$

where the fluid at point 1 is nearly quiescent, and the pressure is assumed to be ambient ($P_1 \approx 0$, $u_1 \approx 0$). At point 2, $P_2 = -P_b$, and the fluid velocity is approximated by the tip velocity of the plate, $u_2 \approx u_T$. Next, the pressure on the front side of the plate is obtained by applying the Bernoulli equation between points 3 and 4 (see figure 9(b)), expressed as:

$$P_{f|S} \sim \rho \left(\frac{R_{rp}^2}{2} \ddot{\theta} + \frac{u_e^2}{2} - \frac{u_T^2}{2} \right), \quad (4.10)$$

where the unsteady term is replaced by its scale and at point 3, $P_3 = +P_f$ and $u_3 \approx u_T$, while at point 4, $P_4 \approx 0$ and $u_4 = u_e$. The jet injection velocity, u_e , in the stationary case, is assumed uniform over the opening width of the clapping cavity for simplification. Similar to (4.6), u_e is obtained using integral mass conservation for a triangular cavity in the lab reference frame: $u_e = R_{rp} \dot{\theta} / 2\theta$. Substituting (4.9) and (4.10) into (4.2), and noting that $\dot{\theta}$ is negligible at the start of rotation of the plate ($u_T \approx 0$ and $u_e \approx 0$), the net mean pressure across the plate in the stationary case is given by:

$$P_{f+b|S} \sim \rho R_{rp}^2 \ddot{\theta}. \quad (4.11)$$

Now, by comparing the expressions for the net mean pressure in the stationary and dynamic cases ((4.11) and (4.8), respectively), we observe that the initial translational acceleration of the body reduces the pressure across the rotating plates in the dynamic case. This reduction leads to a higher rotational velocity of the plates. The behavior can be explained using the rotational equilibrium of the plate, which states that the difference between the applied spring torque and

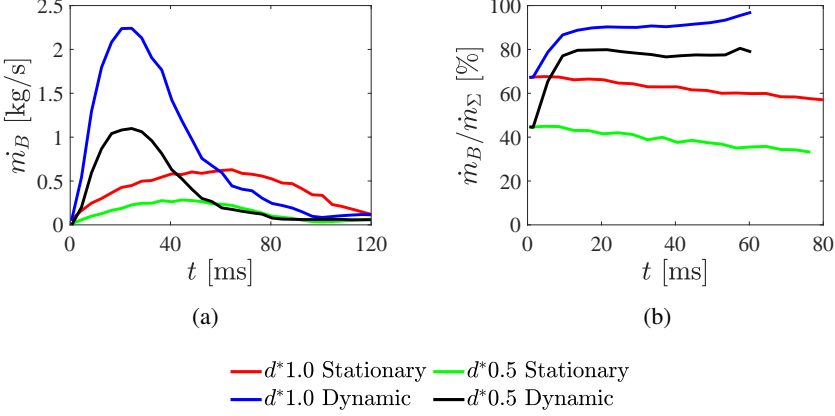


Figure 10: Time variation of the mass flux ejected from the back surface of the interplate cavity, \dot{m}_B : (a) in kg/s and (b) as a percentage of the total mass flux ejected from the interplate cavity, \dot{m}_Σ .

the opposing torque due to pressure forces equals the inertial torque (i.e., the product of the plate inertia and angular acceleration). For a constant spring torque and plate inertia in both cases, the lower pressure in the dynamic case results in a smaller opposing torque. This allows greater angular acceleration in the plates, particularly at the onset of rotation, clearly visible in figure 3(a) as a steeper slope in the $\dot{\theta}$ -vs- t curve for the dynamic case. An alternative explanation for the faster clapping motion in the dynamic cases can be obtained using the potential flow approach during the starting phase of clapping. Following this approach, our previous experimental study (Mahulkar and Arakeri (2024)) modeled the plate motion in the dynamic case as a superposition of rotation and translation. In this superposition, the translational component induces drag on the plate oriented at an angle θ (see figure 8(b)). This drag produces a torque about the hinge point, referred to as drag torque. In the dynamic case, this drag torque acts in the same direction as the spring torque and has comparable magnitude, thereby resulting in faster rotation of the plate. In contrast, in the stationary case, only the spring torque acts, leading to slower rotation.

4.1.2. Mass flux ejected from 3D interplate cavity

A comparison of the flow fields in figures 6c and 6d for stationary and dynamic cases reveals notable differences in the fluid velocities ejected from the interplate cavity. These differences are quantified by measuring the fluid mass flux ejected from the cavity openings. The mass flux ejected from the backside of the cavity, \dot{m}_B ($= \rho \int u_{re} dA_B$), is calculated using the fluid velocity relative to the body, u_{re} , ejected from the rectangular opening area, A_B , at the back. The sideways flux, \dot{m}_S ($= \rho \int u_Z dA_{Top} + \rho \int u_Z dA_{Bot}$), is calculated as the sum of the mass fluxes due to fluid velocity in the Z-direction, u_Z , ejected from the top and bottom triangular areas of the cavity openings, A_{Top} and A_{Bot} , respectively. At the cavity openings, there is a mesh overlap region where area integration causes double counting of cell areas. To avoid this, flux calculations are performed over an area 5 mm away from the rectangular and triangular cavity openings, which does not have mesh overlaps.

The time evolution of \dot{m}_B is shown in figure 10(a) for both d^* values in the stationary and dynamic cases. It exhibits a gradual increase, reaching a peak, followed by a gradual decrease. The maximum value of \dot{m}_B for the stationary cases is 0.28 for $d^* = 0.5$ and 0.63 for $d^* = 1.0$; for the dynamic cases, it is 1.09 for $d^* = 0.5$ and 2.24 for $d^* = 1.0$. This indicates that when the stationary body is allowed to move freely, the maximum \dot{m}_B increases by approximately 3.5 times

for both d^* values. The faster clapping observed in the dynamic cases (figure 3(a)) leads to a more pronounced ejection of mass flux, particularly from the backside. Over the clapping period t_c (see table 1), the evolution of \dot{m}_B as a percentage of the total ejected mass flux, $\dot{m}_\Sigma (= \dot{m}_B + \dot{m}_S)$, reveals a nearly steady trend in both the stationary and dynamic cases, as shown in figure 10(b). In the dynamic cases, as the body begins translating, the ratio \dot{m}_B/\dot{m}_Σ quickly reaches its peak and remains nearly constant throughout the effective clapping duration of 60 ms. The average values of $\overline{\dot{m}_B}/\overline{\dot{m}_\Sigma}$, listed in table 1, are close to 80% for the dynamic cases, suggesting that sideways fluxes are relatively insignificant. In contrast, the proportion of sideways mass flux to total ejected flux, $\overline{\dot{m}_S}/\overline{\dot{m}_\Sigma}$, averaged over the clapping period, is significantly higher in the stationary cases than in the dynamic ones, by a factor of approximately 2.5 for $d^* = 0.5$ and 3.4 for $d^* = 1.0$, see table 1. This increase in sideways flux in the stationary cases can be partially explained by the pressure field shown in figure 6(c). The figure shows that when forward motion is restricted, pressure accumulates on the leading-edge side of the plates, generating a strong lateral pressure gradient along the openings of the interplate cavity, thereby driving significant sideways flow. In contrast, the nearly axisymmetric pressure distribution observed in figure 6(d) for the dynamic case does not produce such a gradient, resulting in negligible sideways ejection. Additionally, within the stationary cases, increasing d^* from 0.5 to 1.0 reduces $\overline{\dot{m}_S}/\overline{\dot{m}_\Sigma}$ by nearly half, from 60.94% to 38.77%, see table 1. This is attributed to the increasing two-dimensionality of the flow field with increasing d^* , where mass flux predominantly exits from the backside opening. Moreover, the prominent sideways flow observed when forward motion of the body is constrained also influences the evolution of wake vortices, which is discussed in the next section.

4.2. Evolution of wake vorticity structures

In our previous experimental study comparing stationary and freely moving clapping bodies (Mahulkar and Arakeri (2024)), we reconstructed an approximate 3D structure of wake vortices using PIV data from two perpendicular planes. However, certain critical aspects of vortex loops, such as their localized curvature, the evolution of their streamwise component during clapping motion, and their behavior near the sharp corners of the clapping plate, remained unknown in the earlier analysis due to the planar nature of the flow field data. In this section, we analyze the evolution of vortex loops in both stationary and dynamic cases for both d^* values, focusing specifically on these aspects.

Figure 11 shows the evolution of wake vortices for the stationary case for $d^* = 0.5$ and $d^* = 1.0$. The figure presents a perspective view of iso-surfaces for vorticity magnitude of 130 s^{-1} at selected time steps, highlighting key stages where the vortices undergo distinct transformations. Additionally, Movies 1 and 2, provided as supplementary material, show the full temporal evolution of vortices in the stationary case for $d^* = 0.5$ and $d^* = 1.0$, respectively. In the stationary cases, the wake vortices evolve through four main phases: one, the development of the starting vortex tube; two, the formation of a weaker stopping vortex tube; three, the emergence of vortex loops due to primary reconnection between the starting and stopping vortex tubes at localized regions; and four, the bridging of vortex loops via secondary reconnection. For $d^* = 0.5$, a detailed discussion on these phases is as follows:

(i) *Starting vortex tube formation phase:* This phase begins with the onset of plate rotation and lasts until approximately 70 ms, just before the end of the rotation at 79.5 ms. During this time, the rotation of the plates generates vorticity, which rolls up to form a starting vortex tube that envelops the top, bottom, and trailing edges of both plates (see figure 11(a)). The vortex tube is colored by the Z-component of vorticity, ω_Z , which clearly reveals opposite signs along the trailing edges of the two plates (red and blue). In contrast, the top and bottom regions of the tube appear green, indicating negligible ω_Z as the vorticity there is predominantly streamwise. To better understand the evolution of streamwise vorticity, ω_X , we show the flow field on a YZ plane located one-third of the plate radius from the trailing edge, see figure 13a. This figure

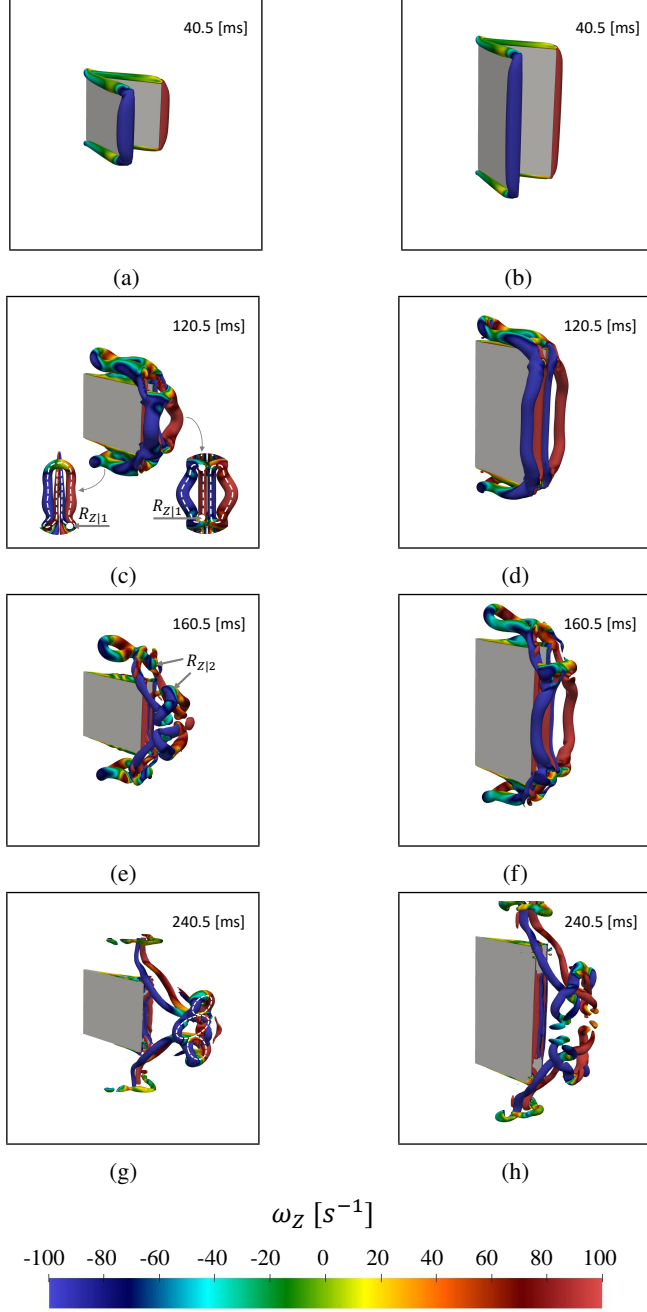


Figure 11: Perspective view of the vorticity iso-surface at a magnitude of 130 s^{-1} , colored with the Z-component of vorticity, ω_Z , for the stationary case with $d^* = 0.5$ (a, c, e, and g) and $d^* = 1.0$ (b, d, f, and h). The inset figure at the bottom right of (c) shows the backside view of the vortex structure spanning the depth, colored with ω_Z . The inset figure at the bottom left of (c) shows the top view of the vortex structure colored with streamwise vorticity, ω_X , where the color legend is the same as for ω_Z , shown at the bottom. In both inset figures, the white-dashed line identifies the vortex loop, and the white circle marks the primary reconnection zone, $R_{Z|1}$. The secondary reconnection zone, $R_{Z|2}$, is marked in (e).

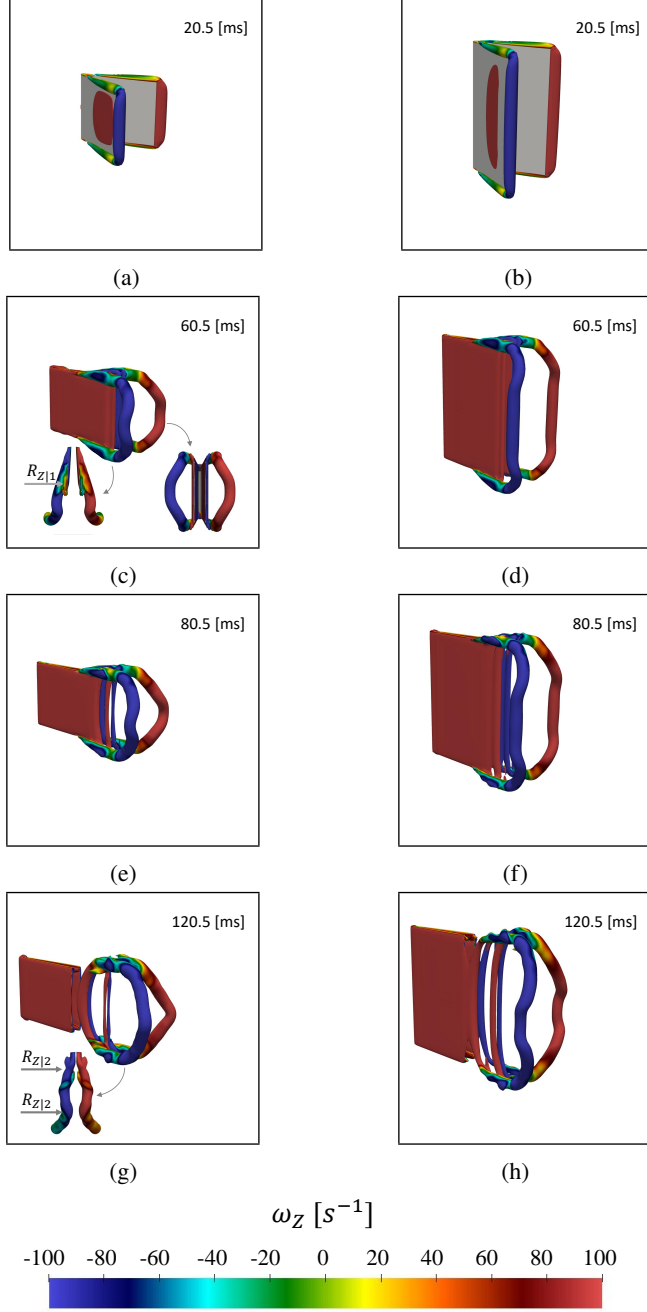


Figure 12: Perspective view of the vorticity iso-surface at a magnitude of 130 s^{-1} , colored with the Z-component of vorticity, ω_Z , for the dynamic case with $d^* = 0.5$ (a, c, e, and g) and $d^* = 1.0$ (b, d, f, and h). In (c) and (g), the inset figure at the bottom left shows the top view of the vortex structure colored with streamwise vorticity, ω_X , with the same color legend as for ω_Z . The inset figure at the bottom right of (c) shows the backside of the wake vortices colored with ω_Z . The primary reconnection zone, $R_{Z|1}$, and the probable sites for secondary reconnection, $R_{Z|2}$, are identified in (c) and (g), respectively.

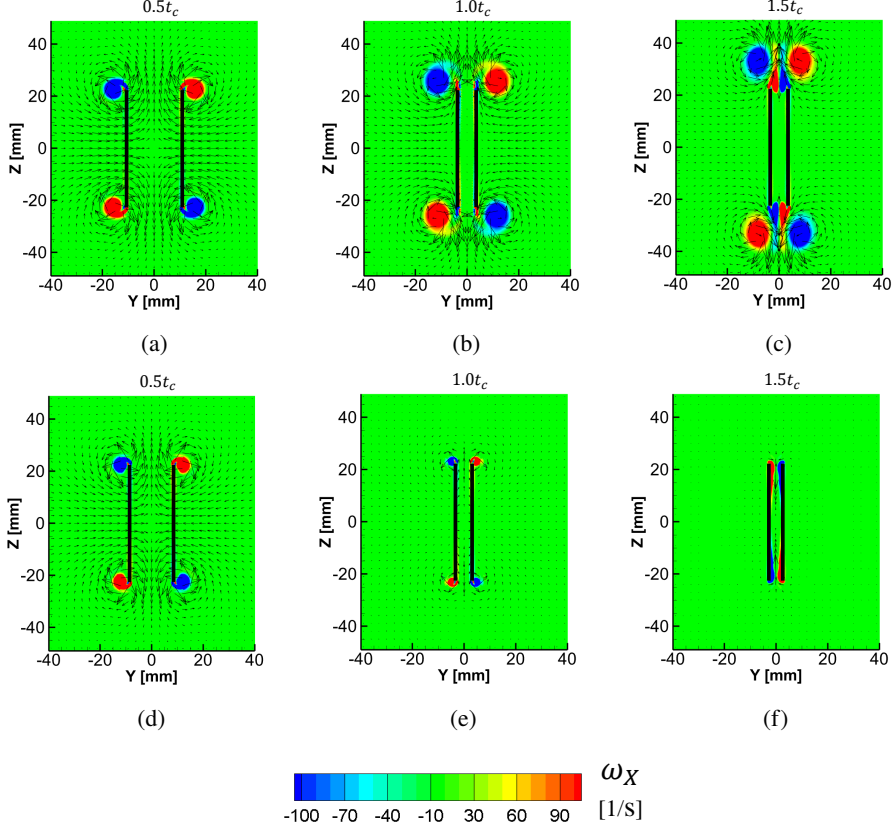


Figure 13: The streamwise vorticity, ω_X , field and velocity vectors on the YZ plane, at one-third of the plate length from the trailing edge. Black lines show the position of the plates. (a), (b), and (c) show the flow field for the stationary case of $d^* = 0.5$, at $t = 0.5t_c$, $t = 1.0t_c$, and $t = 1.5t_c$, respectively, where the clapping period, t_c , equals 79.5 ms. (d), (e), and (f) show the flow field for the dynamic case of $d^* = 0.5$, at $t = 0.5t_c$, $t = 1.0t_c$, and $t = 1.5t_c$, respectively, where $t_c = 67.5$ ms.

shows that, outside the interplate cavity, the flow follows the direction of plate rotation, whereas, inside the cavity, fluid jets are ejected from the top and bottom sides, creating a nearly stagnant zone in the mid-depth region. Simultaneously, outside the cavity, streamwise vorticity rolls up at the top and bottom corners of the trailing edges of both plates (black lines), forming two nearly circular vortex pairs (red and blue in figure 13(a)). These pairs are cross-sections of the starting vortex tubes oriented along the top and bottom edges of the plates. Similarly, the vortex pair observed in figures 4c and d represents the cross-section of the vortex tube along the trailing edges of the plates. Next, we examine the curvature of the vortex tube, which governs its self-induced velocity. The tubes exhibit noticeable curvature: at the top and bottom corners of the leading edges (hinge region); at the top and bottom corners of the trailing edges; and in the mid-depth region of the trailing edges. The highest curvature occurs at the hinge region, where tubes from both plates connect. In contrast, the mid-depth region shows low curvature, while the corners of the trailing edge display intermediate curvature, see figure 11(a). Toward the end of this phase, the high curvature at the hinge region produces a strong self-induced velocity, causing this portion of the tube to move away laterally and transform into a horseshoe-like "U" shaped

vortex. Simultaneously, the vortex tubes in the mid-depth region of the trailing edges lag behind the rotating plates. Their cross-section on the XY plane, shown in figures 4c and d, illustrates this lag. During this time, the curvature at mid-depth increases (e.g., see the vortex structure at 60 ms in Movie 1), producing sufficient self-induced velocity that draws the curved segments of both loops toward each other. Interestingly, despite sharp curvature, the portions of the vortex tubes near the top and bottom corners of the trailing edges remain attached. These corner segments play a critical role in initiating reconnection, which is discussed in a later phase.

(ii) *Stopping vortex tube formation phase*: This phase lasts for a short duration (approximately 70 to 95 ms), during which a thin stopping vortex tube forms along the edges of the plate facing the interplate cavity. The stopping vortex tube essentially forms due to the accumulation of vorticity associated with the deceleration of the rotating plate. The flow field evolution during this phase of stopping vortex formation can be understood from the streamwise vorticity field plotted on the YZ plane, see figure 13(b). The figure shows that, around the end of the clapping motion, the pair of streamwise starting vortices reaches maximum strength, as inferred from their increased cross-section. Simultaneously, very small vorticity patches, oriented opposite to the starting vortices, appear near the top and bottom corners of the trailing edge, indicating the onset of stopping vortex formation. Later, the starting vortices move away from the plate, and the stopping vortices in the interplate cavity become more significant, see figure 13(c). However, the stopping vortices remain much smaller in size due to their confinement within the narrow interplate cavity, which limits vorticity feeding to the vortices. As a result, the stopping vortices remain weaker in strength compared to the starting vortices. These stopping vortices induce flow within the cavity (figure 13(c)), while the stronger starting vortices locally induce flow directed away from the cavity. Apart from this, the flow field is nearly quiescent around the body. At the end of this phase, the thicker starting vortex tube coexists with the thin stopping vortex, see Movie 1.

(iii) *Primary reconnection phase*: In this phase (approximately 95 to 140 ms), the portion of the starting vortex tube attached to the top and bottom corners of the trailing edge comes in very close contact with the stopping vortex tube, initiating local vorticity cancellation. This leads to a significant reduction in the size of the starting vortex tube (see figure 11(c)). Following this interaction, away from the corner regions, the starting and stopping vortex tubes reconnect to form vortex loops on the back, top, and bottom sides of the body. The vortex reconnection is discussed in detail by Melander *et al.* (1989), who numerically studied the cross-linking of two antiparallel vortex tubes. They observed that when the tubes come into close proximity, a bridging region forms in the contact zone, where vorticity reorients perpendicular to the original tube axes. While vorticity is locally annihilated in the contact region, the overall circulation in the bridging portion remains conserved. In the present clapping case, after reconnection, the wake evolves differently on the backside of the body compared to the sideways wake (top and bottom). We first discuss the vortex transformation in the backside wake. Here, the curved starting vortex tube reconnects with the vertical segment of the stopping vortex tube, forming a triangular vortex loop, as indicated by the dashed white line in the bottom-right inset of figure 11(c). For the two plates, the figure shows two triangular loops. In this figure, for clarity, the primary reconnection zone, $R_{Z|1}$, for one plate is marked with a white-filled circle. Note that $R_{Z|1}$ appears at both base corners of the triangular loops for each plate. At $R_{Z|1}$, a green iso-surface ($\omega_Z \approx 0$) indicates the bridging region formed during reconnection. In this portion, the vorticity is reoriented in the perpendicular (Y) direction from its original (Z) alignment in both the starting and stopping vortex tubes. Following Melander *et al.* (1989), we interpret that despite this reorientation, the vorticity strength appears to be largely conserved, as suggested by the finite thickness of the vortex tube in this region. Simultaneous with these backside wake transformations, in the sideways wake, the “U”-shaped starting vortex tube interacts with a sideways-oriented portion of the stopping vortex, leading to reconnection and the formation of a horseshoe vortex resembling an “ Ω ” shape. To visualize this transformation, we include a top view of the vortex structure colored by ω_X , see bottom-left inset

of figure 11(c). In this figure, the dashed white line outlines the “ Ω ” shape, and the white dot marks $R_{Z|1}$, present on both sides of the loop but shown on one side for clarity. Toward the end of this phase, despite the differing evolutions, both the Ω and triangular loops remain connected through a stretched filament of the starting vortex, as shown in figure 11(c). This stretching occurs at the top and bottom corners of the trailing edge, simultaneous to the formation of both loops.

(iv) *Secondary reconnection phase*: This is the final phase of wake vortex evolution, during which the vortex loops interconnect. It begins approximately at 140 ms and continues until the end. We first discuss the vortex transformation that occurs in the backside wake, followed by that in the sideways wake. At the beginning of this phase, in the backside wake, both triangular vortex loops move closer and eventually connect at the corner locations of their bases, forming what we refer to as the secondary reconnection zone, $R_{Z|2}$, as shown in figure 11(e). There are two $R_{Z|2}$ zones: one at the top corner of the interconnected bases and one at the bottom. However, for clarity, only the top $R_{Z|2}$ is identified in this figure. In these reconnection zones, similar to $R_{Z|1}$, a bridge portion develops, with its vorticity oriented perpendicular to the direction of the interconnecting vortex tubes, as highlighted in green in the figure. Once the secondary reconnection forms, the portions of the thin stopping vortex filaments initially located at the bases of the triangular loops come into close contact and undergo annihilation. Such merging of two triangular vortex loops into a single loop was previously observed in the stationary clapping plates study by Kim *et al.* (2013), where they used three-dimensional PIV. Note that in figure 11(e), a discontinuity appears near the apex of the triangular loop, which is a rendering issue in the iso-surface. The iso-surface is plotted at a vorticity value of 130 s^{-1} , but around the secondary reconnection timing, the vorticity in the apex region momentarily spreads over a larger area, dropping below 130 s^{-1} , which manifests as the observed discontinuity. Subsequently, the vorticity reconcentrates in the apex region and the discontinuity disappears (see vortex structure at 185 ms in Movie1). Around this time, the highly curved portions at the apex of both triangular loops rapidly approach each other due to their higher self-induced velocity. This transformation ultimately develops a vortex structure resembling three interconnected ringlets, identified by white dashed lines superimposed on the vortex structure in figure 11(g). A similar three-ringlet structure was observed around 200 ms in our previous experimental study on the clapping body, where a 3D representation of the imagined vortex structure was provided (see figure 15(b) in Mahulkar and Arakeri (2024)). This approximate 3D structure reasonably matches the accurate vortex structure obtained in the present computations. In contrast to the complex transformation in the backside wake, the sideways wake shows a simpler transformation. At the beginning of this phase, the “ Ω ”-shaped horseshoe vortex filament in the sideways wake reconnects in the region $R_{Z|2}$ near the trailing edge, where the filaments were initially in close contact (see figure 11(e)). After this reconnection, one elliptical ringlet emerges from the initial horseshoe vortex in each of the top and bottom side wakes. Subsequently, these ringlets travel and enter the coarse background mesh, where the resolution is insufficient to capture their further evolution. As a result, the ringlets appear as disconnected vorticity patches (see figure 11(g)). So far, we have discussed the formation of three ringlets in the backside wake and two independent ringlets in the sideways wake. As soon as the ringlets form, they convect away from the body due to their self-induced velocity. Interestingly, these ringlets in the backside and sideways wakes remain connected through highly stretched starting vortex filaments, oriented tangentially to the corners of the trailing edges. This completes the discussion of the two-stage reconnection process.

The wake vortex evolution for the stationary case with $d^* = 1.0$, as shown in figures 11(b, d, f, and h) and Movie 2, follows the same four phases as for $d^* = 0.5$, but with a slight delay due to the later closure of the clapping motion ($t_c = 103.5 \text{ ms}$). The first phase of the starting vortex tube formation spans ~ 0 to 100 ms , the second phase of stopping vortex tube formation spans ~ 100 to 120 ms , the third phase of primary reconnection lasts ~ 120 to 180 ms , and the final phase of secondary reconnection continues $\sim 180 \text{ ms}$ until the end of the computation. After the formation

of the starting and stopping vortex tubes, they reconnect around the top and bottom corners of the trailing edges (see figures 11(d, f)). As in the $d^* = 0.5$ case, the primary reconnection in the $d^* = 1.0$ case leads to the formation of an “ Ω ”-shaped vortex loop in the sideways wake. This loop subsequently transforms into an elliptical ringlet through secondary reconnection. In contrast, the vortex evolution in the backside wake of $d^* = 1.0$ follows a slightly different path. Here, two semi-elliptical vortex loops form, with their major axes aligned along the body depth (see figure 11(d)). The main reason for the semi-elliptic shape, as opposed to the triangular-shaped loop for $d^* = 0.5$, is the higher body height, which prevents sharp curvature in the mid-depth region of the vortex loop. Subsequently, both the semi-elliptic loops undergo secondary reconnection at the top and bottom corners of their bases (see figure 11(f)). The reconnection zones $R_{Z|1}$ and $R_{Z|2}$ (not shown) are present on the vortex structure at positions similar to those observed for $d^* = 0.5$. Given the similarity in vortex structure evolution between the two d^* cases with a time delay (for example, figure 11(e) is similar to 11(h)), we expect that both semi-elliptical rings will eventually merge into a single elliptical ring, though this transformation is not captured within the given computation time. Moreover, in the semi-elliptic loops, the absence of sharp curvature at mid-depth prevents the formation of the three-interconnected ringlet structure observed for $d^* = 0.5$. Similar to the $d^* = 0.5$ case, the discontinuity present in the vortex loop in figure 11(h) at the mid-depth region is attributed to the development of lower vorticity values compared to those of the iso-surface plotted. Additionally, our experimental observations validate the hypothesis of the eventual formation of a single elliptical ring in the backside wake, which is observed around 400 ms. Its cross-section on the XZ plane ($Y = 0$) is shown in figure 13(e) of Mahulkar and Arakeri (2024).

When the body is allowed to move freely, the vortices in the wake evolve in a remarkably different manner compared to the stationary cases. See figures 12(a, c, e, and g) and Movie 3 for $d^* = 0.5$, and figures 12(b, d, f, and h) and Movie 4 for $d^* = 1.0$. The time steps in these figures show vorticity structures using the iso-surface of vorticity magnitude 130 s^{-1} , capturing distinctive shape transformations. In contrast to the four-phase evolution observed in the stationary cases, the wake evolution in the dynamic cases follows three phases: first, the formation of the starting vortex tube; second, the shedding of bound vorticity, which occurs simultaneously with primary reconnection that forms vortex loops; and third, secondary reconnection between these loops. We first discuss the phase-wise evolution of the wake vortices for the dynamic case of $d^* = 0.5$ as follows:

(i) *Starting vortex tube formation phase*: This phase spans from 0 to 40 ms. In the beginning (~ 20 ms), as the rotation of the plate dominates over its translation, vorticity rolls up along both side edges (top–bottom) and the trailing edge of both plates, forming the starting vortex tube, see figure 12(a). In this figure, the iso-surface colored with the Z-component of vorticity, ω_Z , shows opposite orientations (red–blue) in the portions of the tube aligned along the trailing edges. However, the portions oriented sideways exhibit streamwise vorticity and therefore show negligible ω_Z (green). The streamwise portion of the vortices is further examined using the ω_X field plotted on the YZ plane, as shown in figure 13(d). During the initial phase of the clapping motion, the flow field inside and outside the interplate cavity, shown in the figure, follows the same pattern as in the stationary case. In this figure, the pairs of streamwise-oriented vortices (red–blue) at the top and bottom sides of the trailing edges represent the cross-section of the starting vortex tubes present along the side edges of the plates. When compared with the stationary case, these pairs are smaller in size, and as time progresses, they become even smaller (see figure 13(e)). This size reduction in starting vortices can be understood from the observation of their 3D structure evolution, towards the end of the formation phase, when the translation of the plate becomes dominant over its rotation (see Movie 2). As a result, the portion of the starting vortex tubes can no longer keep up with the plate’s translation and detaches from its trailing edges. Simultaneously, the streamwise portion of the vortex tube also slides back from its side

edges, preventing streamwise vorticity accumulation over extended periods. Therefore, compared to the stationary case, the shorter time span for vorticity accumulation eventually results in thinner streamwise vortices.

(ii) *Simultaneous bound vorticity shedding and primary reconnection phase*: This phase lasts approximately from 40 ms to 130 ms. At the beginning of this phase, the portion of the starting vortex tube detached from the plate's trailing edge develops noticeable curvature: at the mid-depth and locations that previously rested on the top and bottom corners. See the bottom-right inset of figure 12(c), which shows the backside view of the vortex structure. Simultaneously, the forward motion of the body develops a boundary layer primarily on the outer surface of both plates, as the fluid adjacent to the inner surfaces is trapped within the interplate cavity ($\dot{\theta} \approx 0$). This is in contrast to stationary cases, where the absence of translation does not produce significant vorticity on the outer surfaces of the plates. Therefore, only in dynamic cases do the plates become enveloped with iso-vorticity contours. In this phase, where the plate's translation dominates over its rotation, the vorticity shed from the outer surface of the plate minimally rolls along the side edges of the plate, whereas it predominantly convects downstream from the trailing edges. In the later times, the shed vorticity appears in the form of thin vertical threads just behind the trailing edges, see figure 12(e). In contrast, in the stationary cases, around the stopping time of the plate, the vorticity purely rolls up along the plate's edges in a localized zone, forming the compact stopping vortices. This difference in the vorticity roll-up explains why the stopping vortex formation phase is observed only in the stationary cases. Toward the end of the plate's rotation, primary reconnection occurs along its side edges between the thin bound vorticity tube and the remaining narrow portion of the starting vortex tube, as most of the tube has already detached by this point (figure 12(c)). This reconnection takes place in region $R_{Z|1}$, near the top and bottom corners of the trailing edge of each plate. For clarity, only the top $R_{Z|1}$ of one plate is identified in green in the bottom-left inset of figure 12(c), where the vortex structure is colored by the streamwise vorticity, ω_X . The reconnection forms one vortex loop for each plate, consisting of the starting vortex tube on one side and the shed bound vorticity threads on the other, closer to the body, see figure 12(g). In each loop, the gap between the two bound vorticity threads, one vertical in the central region and the other curved near the trailing edge, corresponds to iso-vorticity values below 130 s^{-1} . By the end of this phase, the wake shows two vortex loops with no interconnection, as clearly illustrated in the bottom-left inset of figure 12(g), which displays a top view of the isolated vortex loops.

(iii) *Secondary reconnection phase*: This phase occurs from 130 ms onward, during which the isolated vortex loops interconnect. Computational data is unavailable for this phase, but based on experimental observations reported in Mahulkar and Arakeri (2024), we discuss further probable transformations in the wake vortices. The secondary reconnection between isolated vortex loops occurs at regions of the loops oriented along the trailing edges (referred to as the backside region) and along the top and bottom side edges (referred to as the sideways region). In the backside region, loops reconnect at three locations of sharp curvature: the mid-depth region and the top and bottom corners (figure 12(g)). At these locations, both vortex tubes approach each other rapidly due to higher self-induced velocity, eventually reconnecting to form two ringlets through three reconnection zones. Simultaneously, in the sideways region, another reconnection occurs in the portions of the vortex loops showing close proximity, see the bottom-left inset of figure 12(g). In this figure, there are two probable secondary reconnection zones, $R_{Z|2}$: one is near the trailing edges of the plates, and another is farther from the trailing edges, around the top corners of the backside region of the vortex loops. Reconnection in these two zones at the top side results in the formation of one elliptical ringlet, and similarly, reconnection at the bottom side also forms one ringlet. Ultimately, reconnection in the backside and sideways regions forms a wake structure of four circumferentially connected ringlets. Such a structure was observed in the experimentally obtained flow field around 200 ms. Its cross-section on the XZ plane ($Y = 0$) is shown in figure

14(c), while its approximate three-dimensional structure is shown in figure 15(d) in Mahulkar and Arakeri (2024). This concludes our discussion of the two-stage reconnection process.

In the dynamic case with increased body depth ($d^* = 1.0$), the wake vortex evolution phases remain the same as those discussed for $d^* = 0.5$. A notable difference is that for $d^* = 1.0$, the backside region of the vortex loops does not exhibit sharp curvature at the mid-depth region (figures 12(d, f)). Due to the absence of such curvature, the vortex loops in this region do not approach each other to reconnect. However, similar to the case of $d^* = 0.5$, at the top and bottom corners of the backside region, the loops come very close to each other, as shown in figure 12(h). Subsequent transformations in the wake vortices are inferred from experimental observations, which span longer durations than the computations. The experiments show that a large elliptical ring appears in the wake around 400 ms, following secondary reconnections at the corners of the backside region of the vortex loops, unlike the two ringlets observed for $d^* = 0.5$. The cross-section of this ring in the XZ plane ($Y = 0$) is shown in figure 14(b) of Mahulkar and Arakeri (2024).

4.3. Wake energy budget

In the previous experimental study on a freely moving clapping body (Mahulkar and Arakeri (2023)), we analyzed the approximate wake energy by assuming it scales similarly to the energy of an axisymmetric thin vortex ring. This approximate analysis provided scaling relations for the body velocity and circulation in the starting vortices, which matched experimental measurements reasonably well and confirmed the energy scaling equivalence between the clapping wake vortices and the axisymmetric thin vortex ring. Interestingly, Sullivan *et al.* (2008) revealed an energy budget deficit in thin vortex rings, generated by impulsively displacing water through a cylindrical nozzle using a piston. Before presenting a detailed discussion of this energy deficit, we first reproduce this aspect of their findings below. They performed experimental measurements of vortex bubble momentum and found it to be equal to the momentum imparted by the piston to the fluid, expressed as $I_\Omega = I_p$. Piston momentum (or slug momentum), $I_p (= m_s u_p)$, calculated as the product of the fluid slug mass, m_s , and piston velocity, u_p , while $I_\Omega (= m_\Omega u_R)$ is the vortex bubble momentum, given as the product of a vortex bubble mass, m_Ω , and vortex velocity, u_R . The experimentally observed momentum conservation between the fluid slug and the vortex bubble implies negligible viscous effects. Furthermore, in an otherwise quiescent domain, the kinetic energy in the vortex bubble, KE_Ω , is expressed as $KE_\Omega = m_\Omega u_R^2 / 2 = I_\Omega^2 / (2m_\Omega)$. Substituting the piston momentum into KE_Ω gives:

$$KE_\Omega = I_p^2 / (2m_\Omega) = (m_s / m_\Omega) KE_p, \quad (4.12)$$

where $KE_p (= m_s u_p^2 / 2)$ is the kinetic energy (or slug energy) added to the fluid by the moving piston. Due to fluid entrainment, the mass of the vortex bubble increases compared to the initial slug mass (Dabiri *et al.* (2004)). Consequently, the kinetic energy in the bubble is lower than the kinetic energy supplied to the fluid ($KE_\Omega < KE_p$). They hypothesized that this difference in energy goes into the formation of the internal structure of the vortex bubble, thereby representing a form of potential energy. It is important to note that this energy budget was evaluated for the flow domain of an isolated vortex ring without a trailing jet. Furthermore, a similar energy deficit is observed in the clapping cases, between the work done on the fluid by the rotating plates and the kinetic energy of the fluid once the wake vortices are fully developed. To better understand this fluid energy budget, we analyze the energy deficit, first, in the simpler wake of a vortex ring (§4.3.1), and later in the more complex wake in the clapping cases (§4.3.2).

4.3.1. Wake energy budget for an axisymmetric vortex ring

A fluid slug discharged through a nozzle or orifice into a fluid domain creates a vortex ring. In this section, we discuss the computation of a vortex ring using a nozzle. The nozzle exit, where

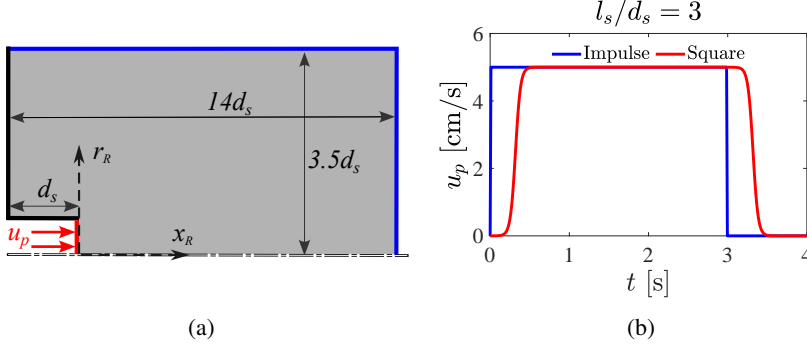


Figure 14: Schematic of the axisymmetric computational domain used for vortex ring generation (not to scale). The domain includes a nozzle that protrudes into the interior, from which a fluid jet with velocity u_p is discharged. Boundary conditions are marked by color: pressure outlet (blue), wall (black), and inlet (red). (b) Two types of time variation programs for the jet injection (or piston) velocity, u_p : Impulse and Square, for $l_s/d_s = 3$.

the fluid velocity is specified, serves as the inlet to an initially quiescent fluid domain. See the axisymmetric computational domain for the vortex ring in figure 14(a), where the nozzle exit is highlighted in red. James *et al.* (1996) and Danaïla *et al.* (2008) used a similar approach to computationally generate a vortex ring. Based on the experimental observations of Gharib *et al.* (1998), the piston stroke-to-diameter ratio ($=l_s/d_s$) is set to 2, 3, and 4 for generating isolated vortex rings, with the piston stroke and diameter assumed equal to the fluid slug length, l_s , and slug diameter, d_s , respectively. We use two types of time variation programs for the piston velocity (also referred to as the jet injection velocity), u_p : impulse and square, as shown in figure 14(b). In the six cases analyzed in this study (two u_p programs for the three values of l_s/d_s), the peak jet injection velocity, u_{pm} , is 5 cm/s, and the nozzle diameter ($=d_s$) is 5 cm, both kept constant. This ensures a constant Reynolds number ($Re_j = u_{pm}d_s/\nu$) of 2500, based on the peak jet injection velocity. At each time instant of u_p , the jet injection velocity profile (spatial variation across the nozzle) is uniform in the impulse program, whereas, in the square program, it follows a hyperbolic tangent profile, as discussed below. James *et al.* (1996) introduced the square program for the jet injection velocity, which we have adopted in this study, given as:

$$\begin{aligned} \frac{u_p(r_s, t)}{u_{pm}} &= \frac{1}{2} (1 - \tanh(10(r_s - 1))) , \quad r_s = 2r_R/d_s, \quad \text{and} \\ \frac{u_p(t)}{u_{pm}} &= \frac{1}{2} \left[\tanh\left(\frac{5}{t_a}(t - t_a)\right) + 1.0 \right], \quad \text{for } t \leq t_a + \frac{t_b}{2}, \\ \frac{u_p(t)}{u_{pm}} &= \frac{1}{2} \left[\tanh\left(\frac{5}{t_a}(t_a + t_b - t)\right) + 1.0 \right], \quad \text{for } t_a + \frac{t_b}{2} < t \leq t_s, \end{aligned} \quad (4.13)$$

where $u_p(r_s, t)$ represents the transient velocity profile (hyperbolic tangent) along the normalized radius of the inlet, r_s , and $u_p(t)$ describes its variation over time, as shown in figure 14(b). The r_s is obtained by normalizing the radial distance along the nozzle, r_R , using half the slug diameter. In the above equations, t_a denotes the acceleration time period of the piston, which is 0.32 s for all three l_s/d_s values. t_b represents the stroke ratio, while t_s is the stopping time of the piston. The t_s is essentially the slug injection time period, calculated based on the slug length, $l_s (= \int_0^{t_s} u_p dt)$. For the square program, t_s is 2.6 s, 3.6 s, and 4.6 s for $l_s/d_s = 2, 3$, and 4, respectively. For the impulse program, t_s is 2 s, 3 s, and 4 s for $l_s/d_s = 2, 3$, and 4, respectively.

In axisymmetric vortex ring computations, the mass and momentum conservation equations

have been solved using ANSYS Fluent. Figure 14(a) illustrates the domain used in these computations. The extent of the fluid domain used is $3.5d_s$ in the radial direction, r_R , and $14d_s$ in the axial direction, x_R . The circular nozzle, $1d_s$ in length, protrudes into the domain from the left, with the origin of the coordinate system positioned at the nozzle exit. In the figure, the pressure outlet boundary condition, highlighted in blue, is applied to the rightmost boundary and the boundary along the axial direction, located $3.5d_s$ from x_R . A wall boundary condition, highlighted in black, is applied to the outer nozzle boundary and the leftmost boundary, which is attached to the nozzle. The inlet boundary condition, highlighted in red, is specified at the nozzle exit, from where a brief discharge of fluid occurs into the domain. For the computation of the vortex ring, we used the same fluid properties, temporal and spatial discretization schemes, and residue criteria as those used for the clapping computations. A time step of 10 ms was chosen to ensure $CFL \leq 0.5$. A mesh independence study was performed using three mesh configurations: a coarse mesh with an element size of 2 mm and a total element count of 30,471; a medium mesh with an element size of 1 mm and a total element count of 1,21,250; and a fine mesh with an element size of 0.5 mm and a total element count of 4,84,997. The meshes were constructed entirely using quadrilateral elements. We compared the mesh types during the vortex formation phase, when vorticity feeding into the ring is complete and the circulation reaches a steady value. The circulation of the ring during this phase, Γ_R , is used as a metric for mesh comparison. $\Gamma_R (= \int \omega_R dA_{cr|R})$ is calculated over the core region, $A_{cr|R}$, where most of the azimuthal vorticity of the vortex ring, ω_R , is concentrated. To identify the core region, Danaila *et al.* (2008) provided a detailed discussion on the vorticity selection criteria. Based on their work, we defined the core region using the criterion: $\omega_R \geq 5\% \omega_{R_{max}}$. For the impulse program of u_p with $l_s/d_s = 3$, the circulation values obtained for the coarse, medium, and fine meshes are $36.443 \text{ cm}^2/\text{s}$, $36.297 \text{ cm}^2/\text{s}$, and $36.452 \text{ cm}^2/\text{s}$, respectively. This shows that the circulation values are almost constant across mesh types. As the difference in the circulation values between the medium and fine meshes is less than 0.5% of the medium mesh value, we used the medium mesh type for the computations of the remaining cases in the parametric space.

We first discuss the flow field for the vortex ring during the formation phase and later validate it with results available in the literature. Figure 15(a) shows the azimuthal vorticity, ω_R , field for an isolated vortex ring generated using the impulse program for u_p with a stroke ratio (l_s/d_s) of 3. The red color in the figure indicates the location of the core center, where vorticity reaches its maximum value. The core region, where most of the vorticity is available, is bounded by the black contour line circumscribing the largest area. The vector field, as shown in this figure, in the lab reference frame, exhibits higher velocity in the central region of the ring, predominantly aligned with the direction of propagation, x_R . Radially away from the vortex core, the flow becomes nearly quiescent, with almost zero vorticity, represented in green. This clearly shows that the flow field is mainly present near the vortex ring. Note that this flow field corresponds to the formation phase, where the circulation becomes steady. The steady state of the vortex ring, over a time period equal to one slug injection time scale, is verified by plotting the nondimensional circulation, Γ_R^* , against nondimensional time, t_R^* (see figure 15(b)). Γ_R^* is obtained by normalizing the ring circulation Γ_R by the slug circulation $\Gamma_s (= 0.5 \int_0^{t_s} u_p^2 dt)$, calculated using the jet injection velocity u_p (see figure 14(b)). Following James *et al.* (1996), we calculate Γ_s using the time variation of the maximum velocity value ($= u_p(t)$) from each of the two profiles: the uniform profile for the impulse program and the hyperbolic profile for the square program. The nondimensional time, $t_R^* = (t - t_{\Gamma_s|R})/t_s$, is measured starting from the ring formation time, $t_{\Gamma_s|R}$, and normalized by the slug injection time, t_s . The values for $t_{\Gamma_s|R}$ are 11 s, 14 s, and 17 s for $l_s/d_s = 2, 3$, and 4, respectively, for both the impulse and square programs. The vortex steady velocity, u_R , normalized with the peak jet injection velocity, $u_{pm} (= 5 \text{ cm/s})$, also verifies the steady nature of the ring over the given duration (see figure 15(b)). Furthermore, the flow field in a reference

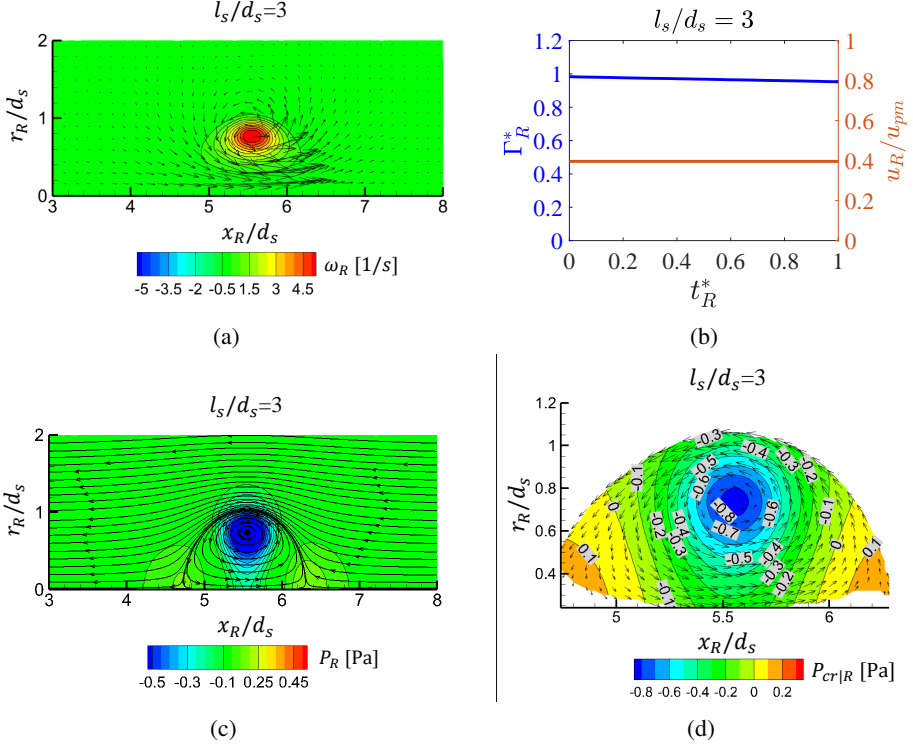


Figure 15: The flow field for an axisymmetric vortex ring generated using the impulse program for u_p for $l_s/d_s = 3$ during the formation phase: (a) Azimuthal vorticity, ω_R , field and velocity vectors in the lab reference frame. (b) Plot of the variation in nondimensional circulation, Γ_R^* , and vortex velocity ratio with nondimensional time, t_R^* . The velocity ratio is obtained by normalizing the steady translational velocity of the vortex ring, u_R , with the peak jet injection velocity, u_{pm} . (c) Streamline plot in the reference frame moving with the steadily translating vortex, and the pressure field in the domain, P_R . The plot shows a cross-section of the vortex bubble, with stagnation points lying on the axis of symmetry, x_R , at the front and backside of the bubble. (d) Pressure field in the vortex core region, $P_{cr|R}$, and velocity vectors in the moving reference frame.

frame steadily moving with the vortex reveals the spheroidal geometry of the vortex bubble, as shown in figure 15(c). In this figure, streamlines are plotted to identify the bubble boundaries. The distance between the two stagnation points, located on the axis of symmetry at the front and back of the bubble, gives the length of the minor axis, $2R_{\min}$. The length scale along the radial direction at the bubble's centroid represents the semi-major axis, R_{\max} . The values of R_{\max} and R_{\min} are provided in table 3. The streamline plot in figure 15(c) is superimposed on the gauge pressure field, P_R , showing maximum negative pressure (blue) in the core region and low-intensity positive pressure (yellow) near the stagnation regions. Note that the initial gauge pressure in the domain was zero. To further examine the pressure in the core region, $P_{cr|R}$, we include a separate plot with a different color legend than that used for the P_R range; see figure 15(d), which reveals an interesting pattern. In the central region of the vortex core, the pressure field shows negative values (blue), transitioning to positive values (yellow-orange) near the axis of symmetry. However, the core can largely be considered a region of negative pressure. This negative pressure plays a crucial role in maintaining the vortex structure. It exerts an inward force on fluid particles, balancing the outward centrifugal force caused by their rotational motion in

l_s/d_s	Program	R_{\max}, R_{\min} [mm]	\forall_{Ω} [cc]	\forall_s [cc]	η_R	$I_{\forall R}$ [gm.m/s]	I_s [gm.m/s]	I_R^*	Γ_R [cm ² /s]	Γ_s [cm ² /s]	Γ_R^*
2	Impulse	47, 34	314.60	196.35	0.38	9.23	9.82	0.94	28.55	25.00	1.14
	Square	45, 33	279.92	196.35	0.30	7.83	9.50	0.82	26.84	24.20	1.11
3	Impulse	51, 39	424.91	294.52	0.31	14.48	14.73	0.98	36.30	37.50	0.97
	Square	49.3, 38	386.87	294.52	0.24	12.50	14.41	0.87	34.32	36.70	0.94
4	Impulse	55.5, 43	554.81	392.70	0.29	19.55	19.63	1.00	42.18	50.00	0.84
	Square	53.4, 42	501.67	392.70	0.22	16.99	19.32	0.88	39.70	49.20	0.81

Table 3: The length of the semi-major axis, R_{\max} , the semi-minor axis, R_{\min} , the volume of the vortex bubble, \forall_{Ω} , the volume of the slug injected into the domain, \forall_s , and the mass entrainment fraction, η_R , are listed in columns 3 to 6 for $l_s/d_s = 2, 3$, and 4, for two types of jet injection velocity programs: impulse and square. The nondimensional momentum values, I_R^* , are listed in column 9, obtained by normalizing the total fluid momentum in the domain, $I_{\forall|R}$, by the slug momentum, I_s . Column 12 shows the nondimensional circulation, Γ_R^* , obtained by normalizing the vortex ring circulation, Γ_R , by the slug circulation, Γ_s .

the core, which is identified by circular streamlines in figure 15(c). Despite its significance, the role of core pressure in the energy budget remains unclear in the literature. We hypothesize that pressure energy is associated with the sustained formation of the vortex core, where an inherently low-pressure region develops from an initial zero-gauge pressure. This pressure energy can be viewed as a form of potential energy linked to the vortex core structure, which must be considered in addition to the kinetic energy in the vortex bubble to resolve the energy deficit discussed in (4.12). Quantitative confirmation of this hypothesis is presented later in this section.

The vortex ring simulations are validated against experimental and computational results from the literature, using three parameters:

- *Fluid entrainment fraction:* Dabiri *et al.* (2004) introduced an entrainment fraction, $\eta_R = 1 - \forall_s/\forall_{\Omega}$, calculated using the volume of the slug, \forall_s , and the volume of the vortex bubble, \forall_{Ω} . For an impulsively moving piston with l_s/d_s values of 2 and 4, they observed that the variation in η_R over time remained nearly steady. The time-averaged values of η_R in their experiments were 0.37 and 0.29 for $l_s/d_s = 2$ and 4, respectively. Our simulations show a close match with these experimental results, giving η_R values of 0.38 for $l_s/d_s = 2$ and 0.29 for $l_s/d_s = 4$, as shown in table 3. In the η_R calculations, the slug volume is given by $\forall_s = \pi d_s^2 l_s/4$, and the volume of the spheroidal vortex bubble is given by $\forall_{\Omega} = 4\pi R_{\max}^2 R_{\min}/3$.

- *Nondimensional wake momentum:* Sullivan *et al.* (2008) measured the vortex bubble momentum for l_s/d_s values of 0.6–1.2 using a ballistic pendulum and found it closely matched the slug momentum. This led to the nondimensional momentum for the ring, $I_R^* (= I_{\forall|R}/I_s) \approx 1$, representing the ratio of the fluid domain (or bubble) momentum, $I_{\forall|R}$, to the slug momentum, I_s . In our axisymmetric domain, we computed the wake momentum as $I_{\forall|R} = \rho \sum u_{xRi} \forall_{Ri}$, where u_{xRi} is the fluid velocity in the axial direction for the i -th cell, and $\forall_{Ri} (= 2\pi y_i dA_i)$ represents the ring volume generated by the i -th mesh cell revolving around the symmetry axis, x_R , with cell area A_i at radius y_i . Similar to Γ_s , the slug momentum, $I_s (= \rho(\pi/4)d_s^2 \int_0^{t_s} u_p^2 dt)$, is computed using the time variation of the maximum velocity ($u_p(t)$ in figure 14(b)), extracted from the uniform and hyperbolic tangent profiles for the impulse and square programs, respectively. The nondimensional momentum, I_R^* , is close to 1 for all l_s/d_s values in the impulse program (see table 3), closely matching the experimental results by Sullivan *et al.* (2008). For the square program, the I_R^* values are slightly lower (0.82–0.88) due to an overestimation of I_s , which arises

from using the maximum velocity of the hyperbolic tangent profile. When the slug momentum is recalculated using the mean velocity of this profile, $\bar{u}_p (= u_p/k_u)$, I_s is reduced by a factor of k_u^2 , where $k_u = 1.035$. This adjustment gives nondimensional momentum values between 0.88 and 0.93.

- *Nondimensional circulation:* For impulsive jet injection, the experimental nondimensional circulation values, $\Gamma_R^* (= \Gamma_R/\Gamma_s)$, reported by Dabiri *et al.* (2004), were 1.34 and 1.12 for $l_s/d_s = 2$ and 4, respectively. These values show a close match with our computational results, where Γ_R^* is 1.14 for $l_s/d_s = 2$ and 0.84 for $l_s/d_s = 4$ (see table 3). Moreover, in 3D vortex ring formation simulations, James *et al.* (1996) found a Γ_R^* of 0.93 for the square program for u_p with $l_s/d_s = 3.3$. This result is in close agreement with our finding of $\Gamma_R^* = 0.94$ for $l_s/d_s = 3$, obtained using an axisymmetric approach.

Following the validation, we now examine the transformation of kinetic energy as the vortex ring forms. The brief initial discharge of the jet into the quiescent fluid introduces kinetic energy (slug energy), which is subsequently transformed as the vortex ring evolves. To analyze this transformation as the vortex ring fully forms, we compute the kinetic energy of the domain as: $KE_{\forall|R} = 0.5\rho \sum |\mathbf{u}_R|_i^2 dV_{R_i}$, where $|\mathbf{u}_R|_i$ is the velocity magnitude at the i -th cell, and dV_{R_i} represents the volume of the ring generated by the revolution of the i -th cell around the axis of symmetry, as discussed earlier. We analyze the time variation in $KE_{\forall|R}$ over the time period equal to one injection time scale ($t_R^* = 1$). During this period, as shown in figure 16(a), the nondimensional kinetic energy $KE_{\forall|R}^* (= KE_{\forall|R}/E_s)$ exhibits steady behavior. It is obtained by normalizing $KE_{\forall|R}$ with the kinetic energy of the slug, E_s , estimated as $E_s = \frac{\pi}{8}\rho d_s^2 \int_0^{t_s} u_p^3 dt$, where $u_p(t)$ represents the time variation in maximum velocity for the square and hyperbolic tangent profiles. For the impulse program of u_p , $KE_{\forall|R}^* \approx 0.6$ for all three l_s/d_s values, see table 4. However, in the case of the square program of u_p , $KE_{\forall|R}^*$ shows slightly lower values (≈ 0.5) due to slug energy overestimation, which arises from using the maximum velocity in the hyperbolic tangent profile. Additionally, the fluid entrainment fraction η_R provides an alternative way to express the ratio of the kinetic energy of the vortex bubble to the kinetic energy imparted to the fluid by the piston. Using (4.12), this energy ratio is given by:

$$\frac{KE_{\Omega}}{KE_p} = \frac{m_s}{m_{\Omega}} = \frac{\forall_s}{\forall_{\Omega}} = 1 - \eta_R. \quad (4.14)$$

For the vortex ring cases studied in this section, $\eta_R \approx 0.3$ (see table 3), resulting in $KE_{\Omega}/KE_p \approx 0.6$. This kinetic energy ratio closely matches $KE_{\forall|R}^*$, confirming that the kinetic energy in the domain, $KE_{\forall|R}$, primarily resides in the vortex bubble, KE_{Ω} , as KE_p represents the slug energy E_s .

We compare the kinetic energy and vortex velocity of the viscous vortex ring with analytical predictions for an inviscid vortex ring. These predictions are based on well-known expressions for the kinetic energy, $KE_{R|inv}$, and steady translation velocity, $u_{R|inv}$, of a thin inviscid ring:

$$KE_{R|inv} = \frac{\rho \Gamma_R^2 R_R}{2} \left[\ln \left(\frac{8R_R}{a_R} \right) - \frac{7}{4} \right], \quad (4.15)$$

$$u_{R|inv} = \frac{\Gamma_R}{4\pi R_R} \left[\ln \left(\frac{8R_R}{a_R} \right) - \frac{1}{4} \right], \quad (4.16)$$

where a_R is the vortex core radius, R_R is the vortex ring radius, and Γ_R is the circulation. A detailed derivation of equations (4.15) and (4.16) is provided in §2.4 of the book on vortex rings by Danaïla *et al.* (2021). The ring radius is determined by identifying the radial location of the vortex core center, where the azimuthal vorticity ω_R reaches its maximum. To extract the vortex core radius, we analyze the tangential velocity u_{θ} of fluid particles moving along circular streamlines within the vortex core. The variation of u_{θ} along the axial line passing through the

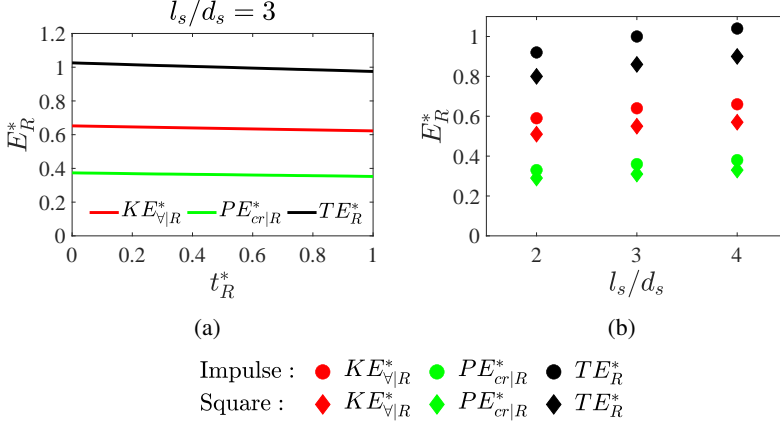


Figure 16: (a) Time variation of nondimensional energy components, collectively denoted by E_R^* : kinetic energy in the full domain $KE_{\forall|R}^*$, potential energy in the vortex core $PE_{cr|R}^*$, and total energy $TE_R^* = KE_{\forall|R}^* + PE_{cr|R}^*$. These are plotted against nondimensional time t_R^* for the impulse program with $l_s/d_s = 3$. (b) Nondimensional energies, averaged over $t_R^* = 1$, plotted against $l_s/d_s = 2, 3$, and 4 for both impulse and square programs. In both figures, the same energy symbols are used since unsteady effects are negligible.

l_s/d_s	Program	t_s [s]	$KE_{\forall R}$ [mJ]	$PE_{cr R}$ [mJ]	E_s [mJ]	$\frac{TE_R}{E_s}$	$\frac{PE_{cr R}}{KE_{\forall R}}$	$KE_{\forall R}^*$	$PE_{cr R}^*$	$PE_{cr +}$ [%]	$PE_{cr -}$ [%]
2	Impulse	2.00	0.15	0.08	0.25	0.93	0.56	0.59	0.33	2.17	97.83
	Square	2.60	0.12	0.07	0.23	0.80	0.56	0.51	0.29	2.41	97.59
3	Impulse	3.00	0.23	0.13	0.37	1.00	0.57	0.64	0.36	3.96	96.04
	Square	3.60	0.20	0.11	0.36	0.86	0.57	0.55	0.31	4.19	95.81
4	Impulse	4.00	0.32	0.18	0.49	1.04	0.57	0.66	0.38	5.04	94.96
	Square	4.60	0.27	0.16	0.48	0.89	0.57	0.57	0.33	5.02	94.98

Table 4: Columns 3 to 7 list the values for the slug discharge period, t_s , kinetic energy in the axisymmetric domain, $KE_{\forall|R}$, potential energy in the core, $PE_{cr|R}$, slug energy, E_s , and the ratio of total energy (sum of kinetic and potential) to slug energy, TE_R/E_s , respectively. The ratio of $PE_{cr|R}/KE_{\forall|R}$, and the nondimensional kinetic and potential energies, $KE_{\forall|R}^*$, $PE_{cr|R}^*$, are given in columns 8 to 10. The last two columns list the values for potential energy in the core region of positive and negative pressure values, $PE_{cr|+}$ and $PE_{cr|-}$, respectively, as a percentage of $PE_{cr|R}$.

core center, with the origin shifted to the axial location of the core center $x_{R|cr}$, is shown in figure 17(a). In this figure, the region marked by dashed lines, where u_θ varies linearly with $x_R - x_{R|cr}$, represents the solid core. The extent of this region defines the solid core diameter, $2a_R$. The computed values of the core and ring radius are listed in table 5. Using these values, we calculate $u_{R|inv}$ and $KE_{R|inv}$. The predicted velocity $u_{R|inv}$ closely matches the measured velocity u_R : $u_{R|inv}/u_R \approx 1$, see table 5. Here, u_R is obtained by differentiating $x_{R|cr}$ with respect to time. However, in contrast to velocity, $KE_{R|inv}$ overestimates the kinetic energy compared to $KE_{\forall|R}$ by approximately 25–30%: $KE_{R|inv}/KE_{\forall|R} = 1.25\text{--}1.32$ (see table 5).

l_s/d_s	Program	R_R [cm]	a_R [cm]	$KE_{R inv}$ [mJ]	$KE_{R inv}/KE_{\forall R}$	$u_{R inv}$ [cm/s]	u_R [cm/s]	$u_{R inv}/u_R$
2	Impulse	3.52	1.38	0.18	1.25	1.78	1.79	1.00
	Square	3.35	1.35	0.15	1.25	1.72	1.75	0.99
3	Impulse	3.87	1.60	0.31	1.32	1.98	2.02	0.98
	Square	3.73	1.65	0.25	1.28	1.93	1.94	1.00
4	Impulse	4.19	1.90	0.42	1.29	2.07	2.10	0.99
	Square	4.03	1.80	0.36	1.32	2.01	2.07	0.97

Table 5: Columns 3 to 6 list the vortex ring radius R_R , core radius a_R , the kinetic energy for the thin inviscid vortex ring $KE_{R|inv}$, and its ratio to the kinetic energy in the viscous domain, $KE_{R|inv}/KE_{\forall|R}$. Columns 7 to 9 show the steady translation velocities for the inviscid and viscous vortex rings, $u_{R|inv}$ and u_R , along with their ratio. The values of $KE_{R|inv}$ and $u_{R|inv}$ are obtained using equations (4.15) and (4.16), respectively.

Around the vortex ring formation time, the ratio of axial momentum in the fluid domain to the slug momentum, I_R^* , remains close to 1 (table 3). This indicates that the momentum of the jet is almost conserved, implying minimal viscous dissipation. Consequently, viscous dissipation of kinetic energy can also be considered negligible. However, $KE_{\forall|R}^*$, approximately equal to 0.6 (table 4), implies that only 60% of the jet’s kinetic energy is retained in the vortex bubble, with the remaining 40% likely transformed into potential energy associated with core formation. We hypothesize that the potential energy in the core, $PE_{cr|R}$, corresponds to the pressure energy obtained by integrating the pressure over the volume of the core region. As previously discussed, the pressure distribution within the core exhibits region-specific values (see figure 15(d)): negative in the solid core region and positive near the axis of symmetry. The pressure energy in these regions is calculated separately as $PE_{cr|-}$ and $PE_{cr|+}$, respectively. Our observations show that, at the formation time, the sum of the magnitudes of $KE_{\forall|R}$, $PE_{cr|+}$, and $PE_{cr|-}$ equals the slug energy, E_s . For example, in an impulse program with $l_s/d_s = 3$, the values are $KE_{\forall|R} = 0.234$ mJ and $PE_{cr|R} = PE_{cr|+} + PE_{cr|-} = 0.134$ mJ, resulting in a total energy $TE_R (= KE_{\forall|R} + PE_{cr|R}) = 0.368$ mJ at formation time, which matches the slug energy, $E_s = 0.370$ mJ, initially added to the domain. Across all l_s/d_s values for the impulse profile, we observed an approximate match between the total energy in the domain and slug energy: $TE_R/E_s \approx 1$, see table 4. Based on these observations, we model the total potential energy in the core as:

$$PE_{cr|R} = \int |P|_{cr|R} d\forall_{cr|R} = \sum |P|_{cr|R_i} d\forall_{cr|R_i}, \quad (4.17)$$

where $|P|_{cr|R}$ represents the magnitude of pressure in the core region, integrated over the core volume $\forall_{cr|R}$. The subscript i denotes quantities for the i -th computational cell, with $\forall_{cr|R_i}$ computed in the same manner as \forall_{R_i} . This model neglects sign variations in the pressure across the core. As shown in table 4 (columns 11–12), the core potential energy $PE_{cr|R}$ primarily arises from negative pressure values, with $PE_{cr|-}$ contributing 95–98% and $PE_{cr|+}$ accounting for only 2–5%. Notably, the potential energy is approximately 60% of the kinetic energy: $PE_{cr|R}/KE_{\forall|R} \approx 0.6$. Furthermore, the core potential energy constitutes 30–40% of the slug energy, with the non-dimensional potential energy $PE_{cr|R}^*$ ranging between 0.3 and 0.4 (see table 4). The $PE_{cr|R}^*$ is obtained by normalizing $PE_{cr|R}$ using E_s . Similar to $KE_{\forall|R}^*$, both $PE_{cr|R}^*$ and the total non-dimensional energy $TE_R^* (= KE_{\forall|R}^* + PE_{cr|R}^*)$ exhibit steady behavior over a period of one t_R^*

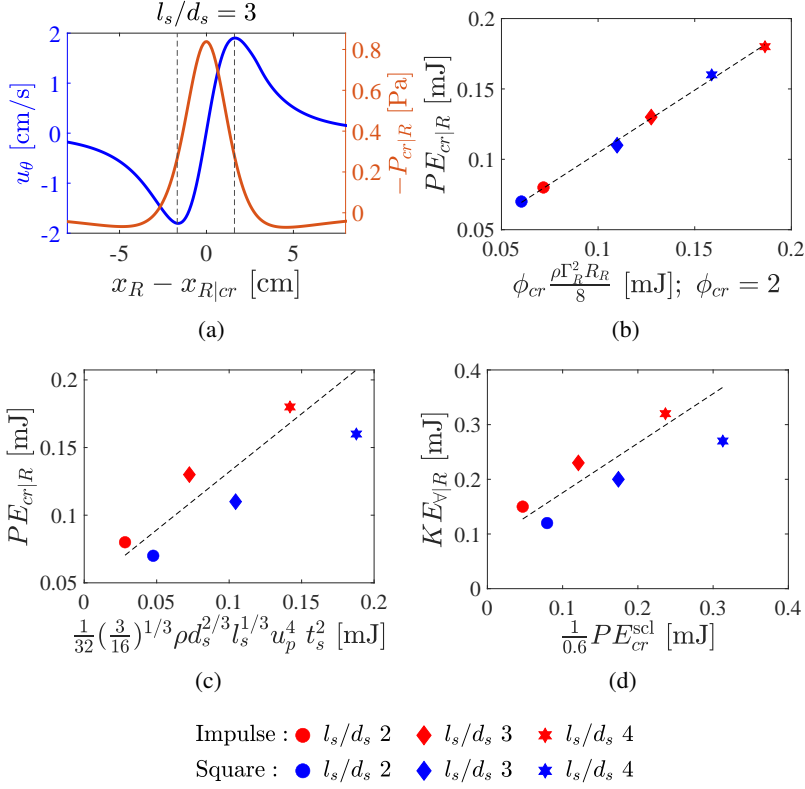


Figure 17: (a) Plot of the tangential velocity, u_θ (blue), of fluid particles traveling along the curved streamlines in the vortex core, and the pressure in the core region, $P_{cr|R}$ (orange), along the axial line passing through the center of the core. For this line, the origin of the axial coordinate, x_R , is shifted to the core center, $x_{R|cr}$. Dotted lines identify the extent of the solid core of the vortex. (b) Potential energy in the core, $PE_{cr|R}$, versus the analytically estimated potential energy, PE_{cr}^a (equation (4.24)), scaled by the core area correction factor, ϕ_{cr} . (c) Potential energy in the core region versus the scale for potential energy, given by (4.28). (d) Kinetic energy in the ring domain versus the scale for kinetic energy, given by (4.29).

(see figure 16). Around the formation time, $TE_R^*(= TE_R/E_s)$ is approximately 1 for all l_s/d_s values in the impulse program. However, for the square program, TE_R^* is slightly less than 1 (see table 4). This discrepancy arises because E_s is overestimated due to using the maximum velocity in the hyperbolic tangent profile. When the mean velocity is used instead, E_s decreases by k_u^3 , leading to $TE_R^* \approx 1$. These results support the core pressure energy hypothesis, demonstrating its role in resolving the energy deficit. It is important to note that this hypothesis has been tested at formation time for $l_s/d_s = 2, 3$, and 4, where the ring naturally forms without a trailing jet. Physically, the potential energy represents a portion of the initial kinetic energy of the jet, which is redistributed to form a stable rotational core zone. This zone maintains relatively low pressure within an otherwise irrotational and quiescent domain at nearly zero gauge pressure.

Using an analytical approach, we derive an expression for the potential energy in the core, as discussed below. For this simplified analysis, we assume that all vorticity is concentrated in the solid core and is uniformly distributed. The pressure within the core region is negative, while it is assumed to be zero outside the core. This pressure distribution assumption is supported

l_s/d_s	Program	$u_{\theta m}^a$ [cm/s]	$u_{\theta m R}$ [cm/s]	$\frac{u_{\theta m}^a}{u_{\theta m R}}$	\bar{P}_{cr}^a [Pa]	$\bar{P}_{cr R}$ [Pa]	$\frac{\bar{P}_{cr}^a}{\bar{P}_{cr R}}$	$2PE_{cr}^a$ [mJ]	$PE_{cr R}$ [mJ]	$\frac{2PE_{cr}^a}{PE_{cr R}}$
2	Impulse	3.29	1.85	1.78	0.27	0.25	1.07	0.07	0.08	0.90
	Square	3.16	1.77	1.79	0.25	0.23	1.08	0.06	0.07	0.86
3	Impulse	3.61	1.90	1.90	0.33	0.27	1.21	0.13	0.13	0.98
	Square	3.31	1.83	1.81	0.27	0.25	1.08	0.11	0.11	1.00
4	Impulse	3.53	1.93	1.83	0.31	0.28	1.12	0.19	0.18	1.04
	Square	3.51	1.87	1.88	0.31	0.27	1.16	0.16	0.16	0.99

Table 6: Columns 3 to 5 list the maximum tangential velocity of fluid particles in the vortex solid core, estimated analytically, $u_{\theta m}^a$, extracted from the computational flow field, $u_{\theta m|R}$, and their ratio. Columns 6 to 8 list the analytically estimated area-averaged pressure in the core region, \bar{P}_{cr}^a , the corresponding value obtained from the simulation, $\bar{P}_{cr|R}$, and their ratio. Columns 9 to 11 show twice the analytically estimated core potential energy, $2PE_{cr}^a$, the corresponding value obtained from the simulation, $PE_{cr|R}$, and their ratio.

by the pressure profile (orange) in figure 17(a), which shows that the negative gauge pressure within the core, marked by the dashed lines, dominates over the near-zero pressure outside. In the same figure, tangential velocity profile (blue) is also shown, where the tangential velocity of fluid particles traveling along curved streamlines, u_{θ} , increases linearly with the radial coordinate of the core, r_{cr} , and is expressed as:

$$u_{\theta}^a = C_u r_{cr}, \quad (4.18)$$

where C_u is a proportionality constant, and the superscript a denotes analytically derived quantities. At the core boundary, $r_{cr} = a_R$, the tangential velocity reaches its maximum value, $u_{\theta m}$. Applying this boundary condition to equation (4.18) gives $C_u = u_{\theta m}/a_R$. Alternatively, this expression for C_u can be rewritten in terms of the circulation in the core, Γ_R . Over the boundary of the solid core, $\Gamma_R (= \int u_{\theta}^a dl_{cr}) = u_{\theta m} 2\pi a_R$, where $l_{cr} = 2\pi a_R$ is the core circumference. From this, we get $u_{\theta m} = \Gamma_R/(2\pi a_R)$. Substituting into the expression for C_u gives $C_u = \Gamma_R/(2\pi a_R^2)$, which, when inserted into equation (4.18), results in:

$$u_{\theta}^a = \frac{\Gamma_R}{2\pi a_R^2} r_{cr}. \quad (4.19)$$

As both Γ_R (table 3) and $a_R (= r_{cr})$ (table 5) are known, this expression provides a prediction for the maximum tangential velocity, $u_{\theta m}^a$. These predicted values are nearly twice the corresponding maximum values extracted from the u_{θ} profiles, $u_{\theta m|R}$ (see column 5 in table 6). This discrepancy is attributed to the fact that u_{θ} does not vary perfectly linearly across the core radius. Nonetheless, the velocity expression remains useful for estimating the mean pressure in the core region, as discussed below. The well-known force balance on an infinitesimally small fluid volume traversing a curved streamline in the core region, is given by:

$$-\frac{\partial P_{cr}^a}{\partial r_{cr}} = \rho \frac{(u_{\theta}^a)^2}{r_{cr}}, \quad (4.20)$$

where P_{cr}^a is the analytically estimated pressure in the core region. This pressure applies a force on the fluid volume that balances the centrifugal force acting on it, maintaining the integrity of the core. Integrating the above equation with respect to r_{cr} , after substituting the expression for

u_θ (4.19), with the boundary condition $P_{cr}^a = 0$ at $r_{cr} = a_R$, gives:

$$P_{cr}^a = \frac{1}{2} \rho C_u^2 (a_R^2 - r_{cr}^2). \quad (4.21)$$

Next, the mean pressure over the core, \bar{P}_{cr}^a , is calculated as $\bar{P}_{cr}^a = (1/A_{cr}) \int P_{cr}^a dA_{cr}$, where $dA_{cr} = 2\pi r_{cr} dr_{cr}$ represents the area of a small ring (annular) element in the circular core. \bar{P}_{cr}^a is then simplified by integrating P_{cr}^a (equation (4.21)) with respect to r_{cr} , which gives:

$$\bar{P}_{cr}^a = \frac{1}{16} \frac{\rho \Gamma_R^2}{\pi^2 a_R^2}. \quad (4.22)$$

In this expression, all the quantities on the right-hand side are known, allowing for the analytical estimation of the mean pressure values. These values closely match the computationally obtained pressure, averaged over the core area, $\bar{P}_{cr|R}$, as shown in column 8 of table 6: $\bar{P}_{cr}^a \approx \bar{P}_{cr|R}$.

We derive an analytical expression for the vortex core potential energy, PE_{cr}^a , using the mean core pressure, \bar{P}_{cr}^a . From equation (4.17), PE_{cr}^a is given as:

$$PE_{cr}^a = \bar{P}_{cr}^a \forall_{cr|R}, \quad (4.23)$$

where $\forall_{cr|R}$ is the toroidal volume of the core, expressed as $\forall_{cr|R} = 2\pi R_R A_{cr}$, with $A_{cr} = \pi a_R^2$. Substituting the expression for \bar{P}_{cr}^a (equation (4.22)), we obtain

$$PE_{cr}^a = \frac{1}{8} \rho \Gamma_R^2 R_R. \quad (4.24)$$

Using known values of Γ_R and R_R , this formula predicts the potential energy in the core, which is found to be nearly half the values obtained from computational data, $PE_{cr|R}$ (see column 11 in table 6, where $2PE_{cr}^a$ is compared with $PE_{cr|R}$). This discrepancy arises primarily due to the larger actual core size (see figure 15(d)) compared to the idealized solid circular core assumed in the analytical model. Based on these observations, we modify PE_{cr}^a by applying a core area correction factor, $\phi_{cr} = 2$. This adjustment gives an expression for the potential energy of the viscous core, $PE_{cr|vis}^a$, as:

$$\boxed{PE_{cr|vis}^a = \frac{1}{4} \rho \Gamma_R^2 R_R}. \quad (4.25)$$

The data plotted in figure 17(b) validate $PE_{cr|vis}^a$ against the computational measurements of potential energy, $PE_{cr|R}$, across the parametric space.

We now present a scaling relation for the potential energy in the vortex core. Following equation (4.24), we begin by determining the characteristic scales for the ring radius and circulation. First, the scale for the ring radius is obtained using a mass conservation relation for the vortex ring, introduced by Sullivan *et al.* (2008), given by:

$$\rho \frac{\pi}{4} d_s^2 l_s \approx \rho \frac{4\pi}{3} R_R^3. \quad (4.26)$$

Here, the left-hand side represents the mass of a fluid slug with diameter d_s and length l_s , while the right-hand side corresponds to the mass of the vortex's inner spheroid. In this analysis, we assume negligible variation in the vortex radius along the major and minor axes of the vortex bubble. Based on this assumption, the scale for the ring radius is:

$$R_{cr}^{scl} \approx \left(\frac{3}{16} d_s^2 l_s \right)^{1/3}. \quad (4.27)$$

With the ring radius scale established, we next obtain a scaling for the circulation. The slug model

gives the circulation scale as $\Gamma_R^{\text{scl}} \approx \frac{1}{2}u_p^2 t_s$, where t_s is the slug injection time and u_p is the jet injection velocity. Substituting the scaling expressions for ring radius and circulation into (4.24), we arrive at the following scale for core potential energy:

$$PE_{cr}^{\text{scl}} \sim \frac{1}{32} \left(\frac{3}{16} \right)^{1/3} \rho d_s^{2/3} l_s^{1/3} u_p^4 t_s^2. \quad (4.28)$$

The scale for the kinetic energy in the domain, $KE_{\forall}^{\text{scl}}$, is estimated using a relation established from computational data, $PE_{cr|R} \approx 0.6, KE_{\forall|R}$ (see column 8 in Table 4), given as:

$$KE_{\forall}^{\text{scl}} \sim \frac{1}{0.6} PE_{cr}^{\text{scl}}. \quad (4.29)$$

The potential energy scaling shows good agreement with the computational data, as illustrated in figure 17(c). Similarly, the kinetic energy predicted by the scale reasonably matches the computational data, as shown in figure 17(d). These scaling relations provide useful estimates for both kinetic and potential energy based on the input parameters for ring generation: l_s , d_s , u_p , and t_s . Note that the derived energy scales have been validated for both impulse and square programs for u_p with $l_s/d_s = 2$ to 4, in the absence of a trailing jet.

4.3.2. Wake energy budget for the clapping body

The reconnection of vortex loops in the clapping cases leads to complex vortex structures, contrasting with the well-defined toroidal structures of the axisymmetric ring. Since both vortex structures are essentially isolated vortex loops in an otherwise quiescent domain, we analyze the energy budget in the clapping wake, following the approach discussed for the axisymmetric ring in the previous section. For the vortex ring, energy transformations are analyzed at the formation time. In the case of the clapping body, the formation time is defined as the time after the clapping motion ends when the wake vortices are fully developed, such that their circulation is steady, and the pressure field predominantly exists in the vortex core, while the pressure field around the clapping body is nearly ambient. The formation time for the clapping vortices, t_{po} , is observed to be 78.5 ms and 90.5 ms for the dynamic cases of $d^* = 0.5$ and 1.0, respectively, and 128.5 ms and 160.5 ms for the stationary cases of $d^* = 0.5$ and 1.0, respectively. For the clapping cases, the kinetic energy in the entire fluid domain, $KE_{\forall|c}$, and the potential energy in the vortex core, $PE_{cr|c}$, as derived from (4.17), are given as:

$$KE_{\forall|c} = \frac{1}{2}\rho \int |u|^2 d\forall_c \quad \text{and} \quad PE_{cr|c} = \int |P|_{cr|c} d\forall_{cr|c}, \quad (4.30)$$

where $|u|$ is the velocity magnitude in the fluid volume within the clapping domain, \forall_c , and $|P|_{cr|c}$ is the absolute value of gauge pressure in the vortex core of volume, $\forall_{cr|c}$. The vortex core region in the clapping wake is identified with the same criteria as that for the axisymmetric ring. In axisymmetric ring formation, a brief jet discharge adds kinetic energy, E_s , to the domain. However, in the case of the clapping body, the unsteady rotation of the clapping plates, driven by the initially applied torque, performs work, $WD_{T|c}$, on the fluid domain:

$$WD_{T|c} = 2 \int_0^{t_c} T_p \dot{\theta} dt \quad \text{and} \quad T_p = 0.5 R_{rp} F_p, \quad (4.31)$$

where T_p is the torque due to the net pressure force, F_p , averaged over the surface area of the plate, which rotates with angular velocity, $\dot{\theta}$, until the end of the clapping motion period, t_c . The force $F_p (= P_{f+b} A_c)$, acting at half the radius of rotation of the rigid plate, R_{rp} , arises from the net pressure, P_{f+b} (see (4.2)), across the plate area A_c . The factor of 2 in the expression for $WD_{T|c}$ accounts for the work done by both plates. Similar to the observation made in the energy budget of the axisymmetric ring, the total energy in the clapping domain, $TE_c = KE_{\forall|c} + PE_{cr|c}$,

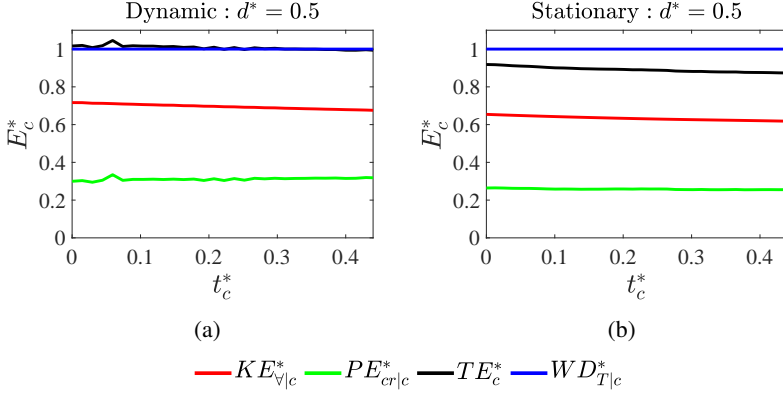


Figure 18: Time variation of nondimensional energies in the clapping domain during the formation phase of wake vortices for (a) dynamic case and (b) stationary case with $d^* = 0.5$. In the figures, $KE_{v|c}^*$, $PE_{cr|c}^*$, TE_c^* , and $WD_{T|c}^*$ represent the nondimensional kinetic energy in the fluid domain, potential energy in the vortex core, total energy (kinetic plus potential), and work done by the plate rotation, respectively.

Case	d^*	$KE_{v c}$ [mJ]	$PE_{cr c}$ [mJ]	TE_c [mJ]	$WD_{T c}$ [mJ]	$\frac{TE_c}{WD_{T c}}$	$KE_{v c}^*$	$PE_{cr c}^*$	$\frac{PE_{cr c}}{KE_{v c}}$
Stationary	0.5	7.08	2.89	9.97	11.19	0.89	0.63	0.26	0.41
	1.0	11.7	6.16	17.86	18.09	0.99	0.65	0.34	0.53
Dynamic	0.5	7.26	3.26	10.52	10.45	1.01	0.69	0.31	0.45
	1.0	13.2	3.92	17.12	15.97	1.07	0.83	0.25	0.30

Table 7: For stationary and dynamic clapping cases of $d^* = 0.5$ and 1.0, the kinetic energy computed over the complete domain, $KE_{v|c}$, potential energy in the core, $PE_{cr|c}$, total energy (sum of kinetic and potential energies), TE_c , work done associated with the unsteady rotation of the plate, $WD_{T|c}$, and the ratio of total energy to work done, $TE_c/WD_{T|c}$, are listed in columns 3 to 7. The last three columns show nondimensional energies: kinetic, $KE_{v|c}^*$; potential, $PE_{cr|c}^*$; and the ratio of potential to kinetic energy, $PE_{cr|c}/KE_{v|c}$, respectively.

around the formation time nearly matches the work added to the fluid domain until the end of the clapping motion: $TE_c/WD_{T|c} \approx 1$, as shown in column 7 of table 7. This demonstrates that the potential energy hypothesis is valid for the wake of the clapping body, despite the wake vortices undergoing reconnection and evolving into complex structures. The key difference compared to the ring case is that, for the clapping cases, the total energy of the domain containing the isolated vortex loops matches the work done $WD_{T|c}$, whereas, for the ring, it is the slug energy that matches the total energy of the vortex loop.

To further examine the time variation in the above-discussed energies, their nondimensional forms ($KE_{v|c}^*$, $PE_{cr|c}^*$, TE_c^*) are plotted against the nondimensional time, t_c^* , see figure 18. For the clapping case, $WD_{T|c}$ is used to normalize the energies as follows: $KE_{v|c}^* = KE_{v|c}/WD_{T|c}$, $PE_{cr|c}^* = PE_{cr|c}/WD_{T|c}$, and $TE_c^* = KE_{v|c}^* + PE_{cr|c}^*$. The nondimensional time is defined as $t_c^* = (t - t_{po})/t_c$, where t_{po} is the formation time and t_c is the clapping period, with t_c values listed in table 1. Figure 18 shows the approximately steady nature of the nondimensional energies

Case	d^*	$I_{m \forall_B}$ [gm.m/s]	$I_{m \forall_B}/d$ [gm/s]	t_{Im} [ms]	$KE_{m \forall_B}$ [mJ]	$KE_{m \forall_B}/d$ [mJ/m]	t_{KE_m} [ms]
Stationary	0.5	7.51	166.8	248.5	2.68	59.6	148
	1.0	17.88	200.8	248.5	6.57	73.8	232
Dynamic	0.5	8.83	196.3	92.5	4.45	98.9	80
	1.0	18.09	203.3	120.5	8.73	98.1	116

Table 8: Columns 3 to 5 list the values for maximum fluid momentum in the negative X-direction, $I_{m|\forall_B}$, integrated over the wake volume, \forall_B (figure 19(b)), its value per unit depth, $I_{m|\forall_B}/d$, and the time when it reaches the maximum value, t_{Im} . The maximum kinetic energy, $KE_{m|\forall_B}$, in the region \forall_B , the energy per unit depth, $KE_{m|\forall_B}/d$, and the corresponding time, t_{KE_m} , are given in columns 6 to 8.

over the chosen timescale of $t_c^* = 0.45$. This timescale was selected to avoid mesh interpolation errors that arise beyond the chosen t_c^* , when the freely moving body transitions from the fine mesh zone, Z_N , to the coarse mesh zone, Z_F (figure 2(b)). By selecting this timescale, we ensure that the energy analysis is performed while the body remains within the fine mesh zone, Z_N . Apart from the steady nature of the energy curves, $TE_c^* \approx 1$ (see also column 7 in table 7) for both the stationary and dynamic cases, indicating that energy loss due to viscous dissipation is negligible over the chosen timescale. Furthermore, momentum conservation between the clapping body and the wake, discussed below, also shows minimal viscous effects. Interestingly, similar to the axisymmetric ring (see table 4), for the clapping cases, $KE_{\forall|c}^* \approx 0.65$ and $PE_{cr|c}^* \approx 0.30$, except for the dynamic case with $d^* = 1.0$, where $KE_{\forall|c}^* = 0.83$ (see table 7). This deviation for $d^* = 1.0$ results from a significant jump in the kinetic energy of the fluid caused by the sudden stopping of plate rotation, which is implemented to prevent complete mesh intersection between the meshes enveloping the plates. This abrupt stop impulsively releases the pressure field generated during plate rotation, creating a favorable pressure gradient that accelerates the fluid and leads to a kinetic energy jump, observed immediately after the rotation halts. In contrast, in experiments, the plate rotation gradually stops, ensuring smooth work-energy transfer. For dynamic cases, when $d^* = 0.5$, the kinetic energy jump is small (about 5% of KE_{\max}), while for $d^* = 1.0$, it is 1.8 mJ (about 13% of KE_{\max}). To account for this significant energy jump in the $d^* = 1.0$ case, we model the total work transferred to the fluid domain as the sum of the plate rotation work, $WD_{T|c}$, and the energy jump, treated as work associated with the sudden stopping of the plates. Note that, in stationary cases, for both d^* values, the energy jump magnitude is negligible, partly due to the lower rotation speed of the plate compared to the dynamic cases. An important point to consider is that volume integration in the overset mesh inherently presents the issue of double-counting cells in overlap zones. In these zones, both solve and donor cells are present, whereas in non-overlap zones, only solve cells exist. The resulting error in energy measurements due to cell double-counting is quantified by separately measuring the energies in the donor cells in the overlap zones. Since the erroneous energy was found to be less than 5% of $KE_{\forall|c}$ and $PE_{cr|c}$ over the specified t_c^* range, this energy error is considered negligible. Additionally, the close match between the work done on the fluid and the total energy in the domain further supports the conclusion that the double-counting errors are negligible.

Modeling the potential energy of wake vortices for the clapping body analytically is challenging, as the vortex volume undergoes significant transient deformations in both the length of the vortex tube and its cross-sectional area. We address this problem using a scaling approach, in which the kinetic energy scale is derived for a simplified 2D wake (see figure 19(a)). This approach leverages

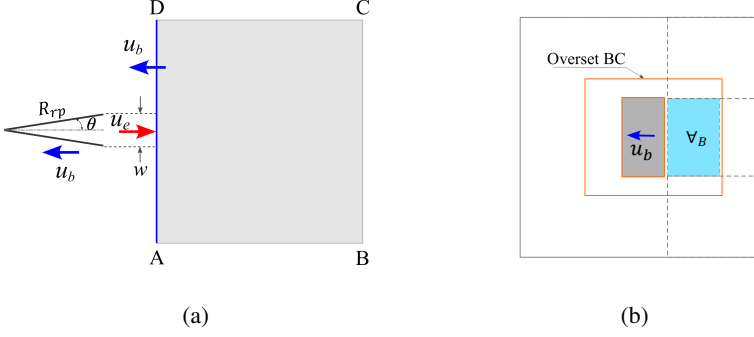


Figure 19: (a) Schematic of the simplified two-dimensional wake, ABCD, of a clapping body. The jet of velocity, u_e , generated due to the closing of an interplate cavity enters the wake from side AD through an aperture of width, w , which is the same as the opening of the clapping cavity. For a clapping body moving with velocity u_b , side AD of the wake follows the body to ensure complete capture of the jet. For forward motion-constrained clapping, side AD remains stationary. (b) Side view of the computational domain for the clapping body showing the wake volume identified in cyan, V_B , lying at the backside of the clapping body. V_B is the depth-wise expansion of the 2D wake region ABCD.

the equivalence of scaling laws for kinetic and potential energy in an axisymmetric vortex ring (see equations (4.28) and (4.29)), whose energy budget is precisely followed by the clapping wake vortices. Before discussing the scaling analysis further, we first examine the momentum and energy values extracted from the computational data of the wake volume, V_B , highlighted in cyan in figure 19(b). Here, V_B represents a depth-wise expansion of the 2D wake. The wake momentum in the direction opposite to that of the body motion, I_{V_B} , and wake kinetic energy, KE_{V_B} , in V_B are defined as:

$$I_{V_B} = \rho \int u_x dV_B, \quad \text{and} \quad KE_{V_B} = \frac{1}{2} \rho \int |u|^2 dV_B. \quad (4.32)$$

where u_x and $|u|$ are the X-component and magnitude of the fluid velocity, respectively, in the domain, V_B , which is large enough to encompass the entire flow field but not extend into overlapping cell regions highlighted in orange in figure 19(b). The wake momentum, I_{V_B} , plotted in figure 20(a), shows a linear increase until the end of the clapping motion ($t = t_c$) in both stationary and dynamic cases for $d^* = 0.5$ and 1.0. Afterward, I_{V_B} continues to increase but at a slower rate in the stationary cases, while maintaining steady values in the dynamic cases. The increase in momentum in stationary cases, occurring after the end of clapping motion, can be understood from flow field observations on the XZ plane, see figures 20(c, d). In these figures, the blue and red vortex patches at the backside of the body represent cross-sections of 3D vortex loops. From 125 ms onwards, these patches grow in size, indicating increased strength. By 230 ms (figure 20d), compared to 125 ms, stronger vortices in the backside wake induce higher velocities, leading to an increase in $I_{m|V_B}$. Note that this growth in vortex core size and strength results from secondary reconnection, as discussed in §4.2. Interestingly, the maximum wake momentum values, $I_{m|V_B}$, are nearly equal in both dynamic and stationary cases (table 8). Although the values rise more gradually in the stationary cases, they still reach their maximum around 248 ms (see figure 20(a)). To better understand the wake momentum, we examine how the clapping motion distributes momentum between the body and the fluid in the wake region for dynamic cases. The clapping action imparts momentum to both the body and the fluid, with the fluid moving in a direction opposite to that of the body. Figure 20(b) shows that the maximum wake momentum in

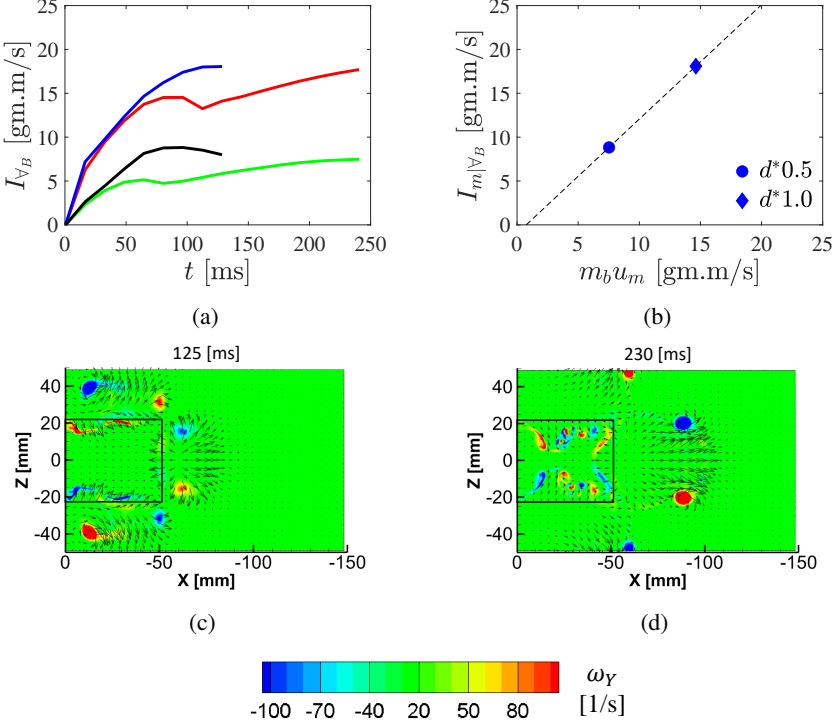


Figure 20: (a) Time variation in fluid momentum in the negative X direction, I_{V_B} , computed over the wake volume V_B at the backside of the body. The legends are the same as shown in figure 3 : blue and black for dynamic cases of $d^* = 1.0$ and 0.5 , respectively; red and green for stationary cases for $d^* = 1.0$ and 0.5 , respectively. (b) Plot of maximum wake momentum, $I_{m|V_B}$, versus the maximum momentum of the freely moving clapping body, $m_b u_m$, for $d^* = 1.0$ and 0.5 , where m_b is the body mass and u_m is the maximum translational velocity of the body. The Y-component of vorticity, ω_Y , is plotted on the XZ plane ($Y=0$) for the stationary body of $d^* = 0.5$ at (c) 125 ms and (d) 230 ms, where the black rectangle shows the body position.

the dynamic cases closely matches the maximum body momentum ($= m_b u_m$) at the end of the clapping motion, when the body of mass m_b reaches its maximum velocity, u_m . In calculating body momentum, we ignored the effect of the surrounding fluid mass, as the body becomes nearly streamlined toward the end of the clapping motion. The sum of the oppositely oriented body and wake momentum, both nearly equal in magnitude, results in a net momentum close to zero, which approximately matches the initial zero momentum when both the body and the fluid were at rest. This verifies the conservation of net momentum, which also implies that viscous effects are negligible over the chosen time period.

The kinetic energy, KE_{V_B} , in V_B , plotted in figure 21, increases almost linearly with time until t_c . Afterwards, KE_{V_B} reaches its maximum value and becomes steady in the dynamic cases. In the stationary cases, following the trend in momentum, KE_{V_B} increases at a slower rate after the initial rapid rise until t_c . The maximum kinetic energy, $KE_{m|V_B}$, in the dynamic cases is slightly higher than in the stationary cases for both d^* values (see table 8). These trends in kinetic energy are valid only when the energy measurements are performed over V_B . When measured over the entire fluid domain, the energy ($KE_{V|c}$) reaches its maximum steady value at the end of the clapping motion, which is nearly identical for both stationary and dynamic cases: approximately

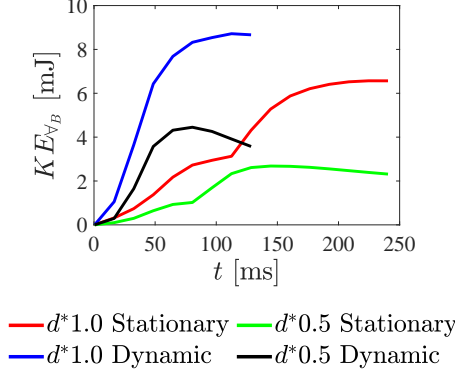


Figure 21: Time variation in kinetic energy, KE_{V_B} , computed over the wake volume, V_B , for stationary and dynamic cases of $d^* = 1.0$ and 0.5 .

7 mJ for $d^* = 0.5$ and 12 mJ for $d^* = 1.0$ (see table 7 and figures 18(a, b)). The difference in $KE_{m|V_B}$ between stationary and dynamic cases is primarily attributed to the strong sideways flow in the stationary case, which reduces the amount of fluid entering V_B . This contrasts with the dynamic cases, where the flow predominantly resides in V_B . As discussed in §4.1.2, this sideways flow varies with d^* in the stationary cases but remains relatively negligible in the dynamic cases. The effect of this sideways flow is more evident in the per-unit-depth energy ($KE_{m|V_B}/d$) and momentum ($I_{m|V_B}/d$), which remain constant with nondimensional depth d^* in the dynamic cases but vary in the stationary cases (see table 8). To visualize the sideways flow, we provide flow field images in figure 22 for $d^* = 0.5$ at the time of maximum kinetic energy, t_{KE_m} , as listed in table 8. These images clearly show prominent sideways flow in the stationary case (figures 22(b, d)). In these figures, the computationally obtained flow field (figures 22(a, b)), when compared with experimental data (figures 22(c, d)), shows an excellent match, capturing even small flow structures near the top and bottom of the trailing edge. This comparison also validates the chosen mesh resolution in the near field of the body. Additionally, figures 22(a, b) reveal the flow structure inside the volume trapped between the plates. In the stationary case, this region is nearly stagnant, while in the dynamic case, it exhibits a wake-like structure as the fluid in the inter-plate cavity is dragged with the moving body. In both cases, inward flow is observed at the top and bottom edges due to streamwise vortices (see also figure 13), which are more pronounced in the stationary case. For further understanding of the flow fields at t_{KE_m} , we provide a plot of the 3D vortex structure superimposed with the velocity vector distribution on the plane of symmetry in figures 22(e, f). Both figures clearly show that the induced velocity from the isolated vorticity structure governs the flow field. In the dynamic case, figure 22(e) shows that 3D vortices sliding back from the moving body induce higher velocities near the top and bottom portions of the vortex loops (red and blue patches in figures 22(a, c)), where the loops come closer together compared to other regions. In the stationary case, shown in figure 22(f), the 3D vortex structure reveals small vortex ringlets at the top, bottom, and backside. These ringlets, formed due to secondary reconnection (as discussed in §4.2), induce higher velocities in their central regions. These regions are identified by larger velocity vectors, marked in red and blue in figures 22(b, d).

We now derive the scaling relations for wake momentum and energy in the 2D clapping wake, as shown in figure 19(a). The wake region ABCD is sufficiently large to encompass the flow field generated by the jet ejected during the clapping motion of plates of radius, R_{rp} , and an inter-plate cavity angle of 2θ . The jet, with velocity, u_e , is ejected from the inter-plate cavity and enters the wake through an aperture of width $w (= 2R_{rp} \sin \theta)$, which is the same as the opening of the

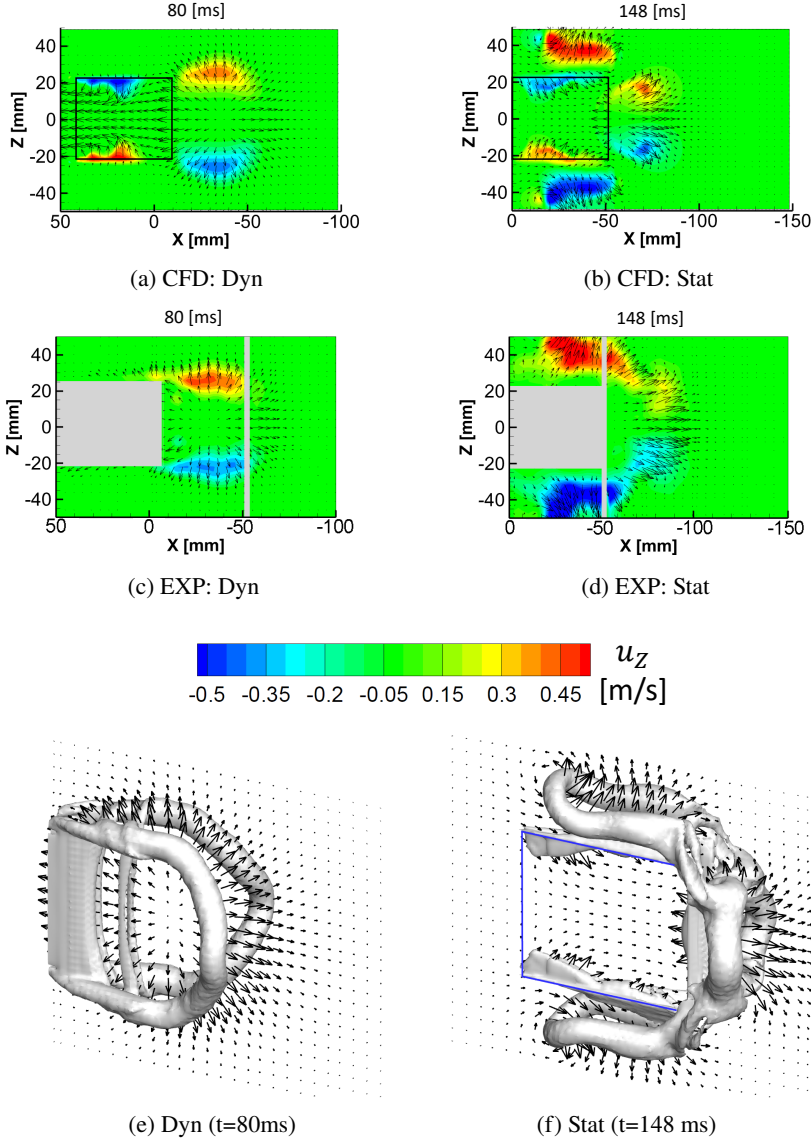


Figure 22: The flow field for the Z-component velocity, u_Z , plotted on the XZ plane ($Y=0$) for the clapping body of $d^* = 0.5$ at the time when KE_{v_B} reaches its maximum value: 80 ms for the dynamic case and 148 ms for the stationary case (table 8). The body position is marked by a black rectangle in the computationally generated (CFD) flow fields for (a) the dynamic (Dyn) and (b) the stationary case (Stat). Experimentally obtained (EXP) flow fields for (c) the dynamic and (d) the stationary case show a close match with the respective computational flow fields; the gray rectangle in both figures shows the shadow region. At the time when kinetic energy reaches its maximum, the iso-vorticity structure at a vorticity magnitude of 130 s^{-1} and velocity vectors on the symmetry plane ($Y = 0$) are shown for $d^* = 0.5$ in (e) the dynamic and (f) the stationary case. In the dynamic case, the vorticity structure in the wake of the freely moving body is shown, whereas in the stationary case, the vorticity structure that remains near the body (blue rectangle) is shown.

clapping cavity. Integral momentum and energy analyses are performed in the lab reference frame over the wake region, which expands in the case of a freely moving body, to ensure complete capture of the jet. For the dynamic case, both the clapping body and side AD (figure 19(a)) of the wake move with velocity u_b , whereas in the stationary case, the wake remains static. Integral momentum conservation in the lab reference frame over the wake region for the stationary case gives:

$$\frac{d}{dt} \frac{I_{c|S}^a}{d} - \rho u_e^2 w = 0, \quad (4.33)$$

where the first term represents the rate of change of the momentum per unit depth in region ABCD, $I_{c|S}^a/d$, obtained analytically (superscript a), and the second term represents the momentum flux entering the wake through the aperture of width w on side AD. In the flux term, u_e is the jet velocity, assumed to be uniform over w . This assumption of uniform jet velocity is used in both energy and momentum analyses for both the stationary and dynamic cases. In this analysis, the wake is assumed to be sufficiently large, such that the velocity flux through sides AB, BC, and CD is negligible. Atmospheric pressure is assumed to act uniformly on all sides of the wake. As discussed earlier, viscous effects are negligible over the time period considered in this clapping computation. Using mass conservation for the inter-plate region (similar to (4.5) and (4.6)), the jet velocity, u_e , in the lab reference frame is expressed as $u_e = R_{rp} \dot{\theta}/2\theta$. Integrating (4.33) over the clapping time period, t_c , and applying small-angle approximations along with the boundary condition $I_{c|S}^a = 0$ at $t = 0$, we get:

$$\frac{I_{c|S}^a(t_c)}{d} = \frac{\rho R_{rp}^3}{2} \int_0^{t_c} \frac{\dot{\theta}^2}{\theta} dt. \quad (4.34)$$

Similarly, using integral energy conservation, the analytical expression for the kinetic energy per unit depth, $E_{c|S}^a/d$, in the wake region ABCD for the stationary case is:

$$\frac{E_{c|S}^a(t_c)}{d} = \frac{\rho R_{rp}^4}{8} \int_0^{t_c} \frac{\dot{\theta}^3}{\theta^2} dt, \quad (4.35)$$

subject to the initial condition of zero kinetic energy. Since all sides of the wake are assumed to be at atmospheric pressure, no work interaction from the wake boundary is included in this expression. For the dynamic case, momentum per unit depth, $I_{c|D}^a/d$, in the lab reference frame over the expanding wake ABCD, obtained using the integral momentum conservation principle, is given as:

$$\frac{d}{dt} \frac{I_{c|D}^a}{d} - \rho u_e (u_e + u_b) w = 0, \quad (4.36)$$

where the first term represents the rate of change of $I_{c|D}^a/d$, and the the second term represents the momentum flux into the domain due to the jet injection with velocity u_e through boundary AD, which moves with velocity u_b in the opposite direction of the jet. Here, $u_e + u_b = u_{re}$ is the relative velocity of the oppositely directed jet with respect to the body. Using the mass conservation equation (4.5), the relative velocity u_{re} is estimated as $u_{re} = R_{rp} \dot{\theta}/2\theta$ (4.6), which leads to the expression for u_e as $u_e = R_{rp} \dot{\theta}/2\theta - u_b$. By substituting the expression for u_e into (4.36) and then integrating over t_c , subject to the initial condition $I_{c|D}^a = 0$ and small-angle approximations, we obtain:

$$\frac{I_{c|D}^a(t_c)}{d} = \frac{\rho R_{rp}^3}{2} \int_0^{t_c} \left(\frac{\dot{\theta}^2}{\theta} - \frac{2}{R_{rp}} u_b \dot{\theta} \right) dt. \quad (4.37)$$

Following the same procedure as for $I_{c|D}^a$, solving the integral energy conservation over the

expanding wake gives the kinetic energy per unit depth in ABCD, $E_{c|D}^a/d$, for the dynamic case as:

$$\frac{E_{c|D}^a(t_c)}{d} = \frac{\rho R_{rp}^4}{8} \int_0^{t_c} \left(\frac{\dot{\theta}^3}{\theta^2} - \frac{4u_b \dot{\theta}^2}{R_{rp} \theta} + \frac{4u_b^2 \dot{\theta}}{R_{rp}^2} \right) dt. \quad (4.38)$$

In both (4.37) and (4.38), viscous effects are ignored, and atmospheric pressure is assumed to act uniformly on all boundaries of ABCD, without contributing any force or work to the wake region.

Further simplification of (4.34), (4.35), (4.37), and (4.38) requires the functional forms of $\dot{\theta}(t)$ and $u_b(t)$, which can be determined using the torque and force equilibrium equations for the clapping plates, respectively. For the stationary case, the torque balance of the rotating clapping plate determines angular acceleration and θ . In the dynamic case, along with the torque equilibrium, the force equilibrium for the translating plate determines linear acceleration and u_b , where thrust on the plate is the horizontal component of the pressure force (see force vectors in figure 8(b)). As discussed in §4.1.1, the pressure field around the body changes significantly during clapping. At the start of plate rotation, the pressure inside the interplate cavity is higher than the outside pressure, but this reverses toward the end of the rotation. This pressure distribution is strongly coupled with the forward motion of the body. Formulating an analytical expression for the pressure across the plate that captures these variations over the clapping period is complex, making it challenging to derive analytical expressions for $\dot{\theta}(t)$ and $u_b(t)$. To address this, we simplify the wake energy and momentum expressions by substituting the scales for u_b , $\dot{\theta}$ and t_c , as described below. From our earlier experimental study on a self-propelling clapping body (Mahulkar and Arakeri (2023)), the scales for maximum body velocity, u_m , and the time at which it is reached, t_{um} , are given as: $u_m \sim \theta_o \sqrt{\frac{2\kappa}{m_b}}$, $t_{um} \sim \sqrt{\frac{2m_b}{\kappa}} \frac{R_{rp}}{\theta_o}$, where κ is the stiffness of the steel plate, θ_o is the initial clapping angle, and m_b is the body mass. In the same experimental study, a linear relationship between the maximum tip velocity, u_{Tm} ($= R_{rp} \dot{\theta}_m$), and u_m was reported as: $u_m = 0.87u_{Tm} + 0.09$, where $\dot{\theta}_m$ is the maximum angular velocity. Using this, the scale for angular velocity becomes $\dot{\theta}_m \sim u_m/R_{rp}$. Furthermore, the experimental study showed that the time at which the body reaches its maximum velocity, t_{um} , closely coincides with the effective clapping period, t_c . Thus, the scales for t_c and t_{um} can be assumed equivalent. In the experimental study comparing dynamic and stationary cases, the nondimensional angular velocities for both cases collapse together (see figures 6(a, b) in Mahulkar and Arakeri (2024)). This suggests that the scales for angular velocity and stopping time for rotation are identical in both cases, allowing the use of scales derived from the dynamic case for $\dot{\theta}$ and t_c in the stationary case. By substituting the scale for u_m as u_b , the scale for $\dot{\theta}_m$ as $\dot{\theta}$, and the scale for t_{um} as t_c into expressions (4.34) and (4.37), the wake momentum per unit depth for stationary and dynamic cases becomes:

$$\frac{I_{c|S}^a}{d} \sim \rho R_{rp}^2 \sqrt{\frac{2\kappa}{m_b}}, \quad \text{and} \quad \frac{I_{c|D}^a}{d} \sim \rho R_{rp}^2 \sqrt{\frac{2\kappa}{m_b}} (1 - 2\theta_o), \quad (4.39)$$

respectively. Similarly, from equations (4.35) and (4.38), the wake energy per unit depth for stationary and dynamic cases is:

$$\frac{E_{c|S}^a}{d} \sim \frac{\rho R_{rp}^2}{2} \frac{\kappa}{m_b}, \quad \text{and} \quad \frac{E_{c|D}^a}{d} \sim \frac{\rho R_{rp}^2}{2} \frac{\kappa}{m_b} (1 - 2\theta_o)^2, \quad (4.40)$$

respectively. The only difference between the scales for stationary and dynamic cases is the additional factor of $(1 - 2\theta_o)$ in the latter. Ignoring this constant factor, the scales for wake

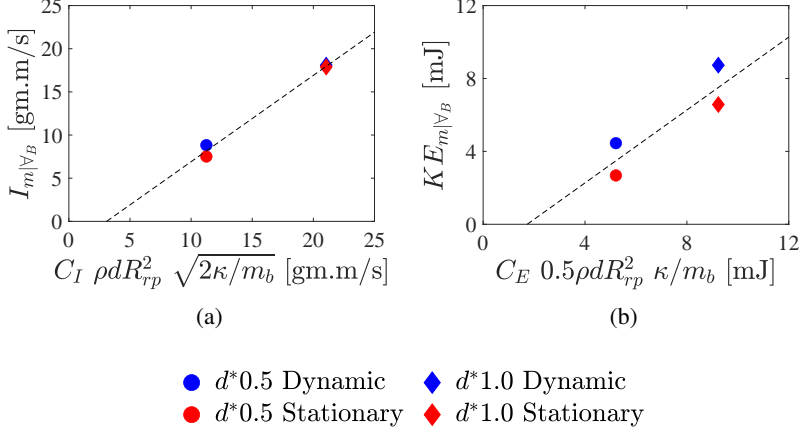


Figure 23: (a) Maximum wake momentum, $I_{m|\nabla_B}$, versus the scaled wake momentum, I_c^{scl} , multiplied by the curve fitting coefficient, C_I . (b) Maximum wake energy, $KE_{m|\nabla_B}$, versus the scaled wake energy, E_c^{scl} , multiplied by the curve fitting coefficient, C_E .

momentum and energy are:

$$I_c^{\text{scl}} \sim \rho d R_{rp}^2 \sqrt{\frac{2\kappa}{m_b}}, \quad \text{and} \quad E_c^{\text{scl}} \sim \frac{\rho d R_{rp}^2}{2} \frac{\kappa}{m_b}, \quad (4.41)$$

respectively.

Note that the scales I_c^{scl} and E_c^{scl} estimate the wake momentum and energy, respectively, for the wake volume ABCD with depth d (figure 19a). These scales are derived under the assumption that the jet velocity entering the wake region is uniform over this depth. However, computational observations show that the fluid jet velocity in the negative X-direction at the backside opening of the interplate cavity decreases toward the top and bottom sides of the clapping plate of depth d (see figures 6(c, d)). As a result, the wake momentum and energy values estimated using these scales are higher than those obtained from computational data in the wake volume ∇_B (figure 19b). To correct for this overestimation, I_c^{scl} is compared with the maximum wake momentum, $I_{m|\nabla_B}$, and E_c^{scl} is compared with $KE_{m|\nabla_B}$. Using a curve-fitting approach, this comparison estimates the correction coefficients C_I and C_E for the momentum and energy scales, respectively. After applying the correction coefficients, both wake momentum and energy scales show a linear trend with d^* : see figure 23a, where the momentum scale is multiplied by the coefficient $C_I = 0.033$, and figure 23b, where the energy scale is multiplied by the coefficient $C_E = 0.022$. In these plots, for $d^* = 1.0$, $\kappa = 72.6 \text{ mJ/rad}^2$ and $m_b = 21.2 \text{ gm}$; for $d^* = 0.5$, $\kappa = 40.5 \text{ mJ/rad}^2$ and $m_b = 10.6 \text{ gm}$. For a first-order understanding, these scales reveal that wake momentum and energy primarily depend on the square of the radius of rotation of the plate and its stiffness, while being inversely proportional to body mass.

5. Concluding remarks

We report a computational study on clapping propulsion, performed using a body that essentially consists of two thin rigid plates hinged together at one edge, forming an interplate angle of $2\theta_o = 60^\circ$ (figure 2a). Upon actuation, the cavity between the plates closes, ejecting a thrust-producing fluid jet. For two aspect ratios, $d^* = 0.5$ and 1.0 , the plate motion data is taken from our previous experimental study (Mahulkar and Arakeri, (2024)) for two cases: the

dynamic case, where the body moves forward while the interplate cavity closes, and the stationary case, where the body's forward motion is constrained while the cavity closes. The experiments revealed surprising differences in the near-body and wake flow fields between these cases. The present study aims to understand these differences using three-dimensional flow fields obtained from simulations. These simulations are performed in ANSYS-Fluent using overset meshing to account for large mesh displacements associated with the body's translation and the severe contraction of the interplate cavity. The computed flow structures closely match the experimental flow field obtained using 2D PIV (figure 4). Furthermore, for a quantitative comparison between simulations and experiments, we used the circulation of the starting vortex, formed during the rotation of each clapping plate. The comparison reveals slightly lower circulation values in the experiments compared to the simulations (figure 5). This difference is attributed to vorticity contributions from flow over a 2 mm thick balsa piece (shown at the backside of the clapping plates in figure 1), which cancels part of the vorticity forming the starting vortex in the experimental flow field. In contrast, this effect is negligible in the simulations, where the plates are flat.

With the model validated, we next examine the near-body pressure field to understand how it varies between the stationary and dynamic clapping cases. In the stationary case, pressure is higher on the side of the rotating plate facing the cavity and lower on the backside (figure 6a). In contrast, the dynamic cases exhibit lower overall pressure values in the near-body field, although the pressure distribution across the plate remains approximately similar (figure 6b). In the initial phase of clapping, (4.8) shows that forward acceleration of the body primarily reduces pressure values in the dynamic case, as derived using the unsteady Bernoulli equation. This reduction in pressure across the plates decreases the pressure-torque that opposes plate rotation. As a result, for a constant applied torque on the plate, the lower opposing torque in dynamic cases leads to a larger angular acceleration at the onset of plate rotation, as observed in the experiment (figure 3(a)). Furthermore, the evolution of the pressure field is quantified using the thrust coefficient, C_T , which shows higher values for the stationary case (figure 7a). As the body begins moving forward, C_T drops sharply as part of the reactive force initially available with the water is transferred to the translating body. Additionally, in the stationary case, a stronger pressure gradient at the sideways opening generates significant lateral flows, although this effect decreases as body height increases. The sideways mass flux, averaged over the clapping period, is almost three times higher in the stationary case compared to the dynamic case.

We now describe how the wake differs between the stationary and dynamic cases in terms of the formation and evolution of vortices, based on 3D vorticity data. In the stationary cases, for each plate, the vorticity field shows that as plate rotation begins, a starting vortex tube forms, enveloping the edges of the plate. This is followed by the formation of a stopping vortex tube during the retardation phase of plate rotation. Subsequently, at the top and bottom corners of the trailing edge on both plates, the stronger starting vortex tube comes into close contact with the weaker stopping vortex tube, resulting in vorticity cancellation and a reduction in the strength of the starting vortex tube. Away from the corners, the primary reconnection occurs between both vortex tubes, forming two triangular loops (one for each plate, as shown in the bottom-right inset of figure 11c) in the backside wake of the interplate cavity. Along with the triangular loops, one horseshoe-shaped vortex loop forms in the topside wake, and another forms in the bottomside wake of the cavity. Later, secondary reconnection occurs in the vortex loops (figure 11g), separately at the backside and sideways (top and bottom sides) wakes. Interestingly, this description of wake evolution in the stationary case changes significantly right from the onset in the dynamic case. In dynamic cases, for each plate, the starting vortex tube forms at the beginning of rotation but slides back as the body translates forward. Toward the end of clapping, the starting vortex tubes reconnect with the bound vorticity threads shed from the outer surfaces of the translating plates, forming an elliptical ring for each plate (figures 12g and h), which eventually undergoes secondary reconnection. The key differences in vortex evolution for dynamic cases, compared to stationary

cases, include negligible sideways flow, which prevents ringlet formation at the top and bottom of the cavity, and the near absence of stopping vortices due to the translation of the plates. Notably, in both stationary and dynamic cases, for both d^* values, vortices ultimately evolve into isolated structures without a trailing jet.

In the isolated vortices, a deficit in the energy budget was previously reported by Sullivan *et al.* (2008). In their experiments on isolated vortex rings, they found that when the vortex bubble develops perfectly, its momentum nearly equals the momentum of the slug injected into the domain, implying negligible viscous effects. However, its kinetic energy is less than the slug's kinetic energy. They hypothesized that this missing energy must be invested in the formation of the vortex structure. To investigate this further, we performed axisymmetric simulations of vortex rings for stroke-to-diameter ratios of 2, 3, and 4, with a nozzle diameter of 5 cm and a Reynolds number based on jet velocity of 2500. Two types of velocity injection programs were used: impulse and square (figure 14b), with a maximum jet injection velocity of 5 cm/s. At the time of vortex formation, the computational data shows that the total momentum in the domain, in the direction of ring propagation, matches the slug momentum, while the kinetic energy in the domain is approximately 60% of the slug's energy (figure 16). For the remaining 40% of the energy, our hypothesis is that it is potential energy invested in the formation and maintenance of the vortex structure. We compute this energy by integrating pressure values over the vortex core region (4.17), and its magnitude closely matches the energy deficit values for all cases considered in this study. Furthermore, an analytical expression (4.25) is derived for the potential energy associated with the core of uniform vorticity, where the pressure inside the core is negative and the pressure outside is ambient (zero gauge). Additionally, scaling laws (4.28) and (4.29) are derived for the potential and kinetic energies of the vortex ring, respectively, enabling energy calculations using initial parameters for vortex ring generation: nozzle diameter, stroke length, injection time, and fluid density.

The isolated wake vortices, as discussed above, in both stationary and dynamic clapping cases follow the energy budget equivalence with the axisymmetric vortex ring. In both cases, the sum of the kinetic energy in the domain and the potential energy associated with the core equals the net work done on the fluid by the clapping plates (figure 18), with the work calculated by integrating the product of pressure torque on each plate and its angular velocity over the clapping period. This budget is analyzed at the formation time, defined as the period after clapping ends, when the pressure field around the plates becomes negligible. Furthermore, the scaling laws for clapping wake momentum and energy, as given by (4.41), are derived for a simplified 2D wake region using integral momentum and energy conservation principles, respectively. Note that the concept of potential energy in the vortex core, introduced in this study, has been verified for isolated vortex loops of circular and irregular shapes. However, for vortex rings with a trailing jet, this concept requires further investigation.

Appendix A. Unsteady Bernoulli equation in a non-inertial frame

We begin with the Euler momentum equation for a small fluid element in a non-inertial reference frame. For incompressible and inviscid flow, the equation is given by

$$\frac{\partial \mathbf{u}_r}{\partial t} + (\mathbf{u}_r \cdot \nabla) \mathbf{u}_r = -\frac{\nabla P}{\rho} - \mathbf{a}_F, \quad (\text{A } 1)$$

where \mathbf{u}_r is the fluid velocity in the moving (non-inertial) frame, ρ is the fluid density, P is the static pressure, and ∇ is the spatial gradient operator. The term \mathbf{a}_F represents the acceleration of the reference frame, which introduces a fictitious body force acting on the fluid element. Note that boldface symbols are used to denote vectors. Now, for inviscid and irrotational flow, the velocity can be expressed as $\mathbf{u}_r = \nabla \phi$, where ϕ is the velocity potential. Applying the identity

$\nabla(\mathbf{u}_r \cdot \mathbf{u}_r) = 2(\mathbf{u}_r \cdot \nabla)\mathbf{u}_r + 2\mathbf{u}_r \times (\nabla \times \mathbf{u}_r)$, and noting that $\nabla \times \mathbf{u}_r = \mathbf{0}$ in potential flow, equation (A 1) simplifies to:

$$\frac{\partial}{\partial t} \nabla \phi + \frac{1}{2} \nabla(\nabla \phi \cdot \nabla \phi) + \frac{\nabla P}{\rho} + \mathbf{a}_F = 0. \quad (\text{A } 2)$$

Next, we integrate (A 2) along a streamline from point 1 to point 2. Since the flow direction follows the streamline, the velocity potential gradient simplifies to $\nabla \phi = \frac{\partial \phi}{\partial s} \mathbf{e}_s$, where s is the arc length along the streamline and \mathbf{e}_s is the unit tangent vector. This leads to:

$$\int_1^2 \frac{\partial}{\partial s} \left(\frac{\partial \phi}{\partial t} + \frac{1}{2} \nabla \phi \cdot \nabla \phi + \frac{P}{\rho} \right) \mathbf{e}_s \cdot d\mathbf{s} + \int_1^2 \mathbf{a}_F \cdot d\mathbf{s} = 0. \quad (\text{A } 3)$$

Here, the first term is recognized as the local unsteadiness along the streamline:

$$\frac{\partial}{\partial t} \left(\frac{\partial \phi}{\partial s} \right) \mathbf{e}_s = \frac{\partial \mathbf{u}_r}{\partial t}. \quad (\text{A } 4)$$

Moreover, for a freely moving clapping body, the frame acceleration, \mathbf{a}_F , is the same as the translational acceleration of the body, $\dot{\mathbf{u}}_b$. Substituting these into equation (A 3), we get the unsteady Bernoulli equation in a non-inertial frame:

$$\boxed{\int_1^2 \frac{\partial \mathbf{u}_r}{\partial t} \cdot d\mathbf{s} + \int_1^2 \dot{\mathbf{u}}_b \cdot d\mathbf{s} + \frac{P_2}{\rho} + \frac{u_{r2}^2}{2} = \frac{P_1}{\rho} + \frac{u_{r1}^2}{2}.} \quad (\text{A } 5)$$

Acknowledgements

The authors are grateful to Prof. Gaurav Tomar (IISc, Bangalore) for the insightful discussions during the initial phase of the project. We sincerely thank Prof. Pramod Kumar and Prof. Susmita Dash (IISc, Bangalore) for providing the Ansys-Fluent software.

REFERENCES

- BARTOL, I. K., KRUEGER, P. S., STEWART, W. J., & THOMPSON, J. T. 2009 Hydrodynamics of pulsed jetting in juvenile and adult brief squid *Lolliguncula brevis*: evidence of multiple jetmodes' and their implications for propulsive efficiency., *J. Expl Biol.*, **212**, pp.1889-1903.
- BARTOL, I. K., KRUEGER, P. S., JASTREBSKY, R. A., WILLIAMS, S., & THOMPSON, J. T. 2016 Volumetric flow imaging reveals the importance of vortex ring formation in squid swimming tail-first and arms-first., *J. Expl Biol.*, **219**, pp.392-403.
- BUJARD, T., GIORGIO-SERCHI, F., & WEYMOUTH, G. D. 2021 A resonant squid-inspired robot unlocks biological propulsive efficiency., *Science Robotics*, **6(50)**.
- BRODSKY, A. K. 1991 Vortex Formation in the Tethered Flight of the Peacock Butterfly *Inachis io* L. (Lepidoptera, Nymphalidae) and some Aspects of Insect Flight Evolution., *J. Exp Biol*, **161**, pp. 77-95.
- CHENG, M., LOU, J., & LIM, T. T. 2018 Numerical simulation of head-on collision of two coaxial vortex rings, *Fluid Dyn. Res.*, **50**, 065513.
- DABIRI, J. O., & GHARIB, M. 2004 Fluid entrainment by isolated vortex rings., *J. Fluid Mech.*, **511**, pp. 311-331.
- DABIRI, J. O., COLIN, S. P., COSTELLO, J. H., & GHARIB, M. 2005 Flow patterns generated by oblate medusan jellyfish: field measurements and laboratory analyses., *J Exp Biol*, **208**, pp.1257-1265.
- DABIRI, J. O., COLIN, S. P., & COSTELLO, J. H. 2006 Fast-swimming hydromedusae exploit velar kinematics to form an optimal vortex wake., *J Exp Biol.*, **209**, pp.2025-33.
- DANAILA, I., & HÉLIE, J. 2008 Numerical simulation of the postformation evolution of a laminar vortex ring., *Physics of Fluids*, **20(7)**.
- DANAILA, I., KAPLANSKI, F., & SAZHIN, S. S. 2021 Vortex ring models., *Springer*.

- DAS, P., GOVARDHAN, R., & ARAKERI, J. 2013 Effect of hinged leaflets on vortex pair generation., *J. Fluid Mech.*, **730**, pp.626-658.
- DAS, P., GOVARDHAN, R., & ARAKERI, J. 2018 Unsteady two-dimensional jet with flexible flaps at the channel exit., *J. Fluid Mech.*, **845**, pp.462-498.
- EPPS, B. P. 2010 An impulse framework for hydrodynamic force analysis: fish propulsion, water entry of spheres, and marine propellers., *PhD Thesis, MIT*, pp.40.
- GHARIB, M., RAMBOD, E., & SHARIFF, K. 1998 A universal time scale for vortex ring formation., *J. Fluid Mech.*, **360**, pp.121-140.
- JAMES, S., & MADNIA, C. K. 1996 Direct numerical simulation of a laminar vortex ring., *Physics of Fluids*, **8(9)**, pp.2400-2414.
- DAVID, M. J., MATHUR, M., GOVARDHAN, R. N., & ARAKERI, J. H. 2018 The kinematic genesis of vortex formation due to finite rotation of a plate in still fluid., *J. Fluid Mech.*, **839**, pp.489-524.
- GEMMELL, B. J., DABIRI, J. O., COLIN, S. P. COSTELLO, J. H., TOWNSEND, J. P., & SUTHERLAND, K. R. 2021 Cool your jets: biological jet propulsion in marine invertebrates., *J. Exp Biol.*, **224(12)**, pp.jeb222083.
- JOHANSSON, L. C., & HENNINGSSON 2021 Butterflies fly using efficient propulsive clap mechanism owing to flexible wings., *J. R. Soc. Interface*, **18**, 20200854.
- KIM, D., HUSSAIN, F., & GHARIB, M. 2013 Vortex dynamics of clapping plates., *J. Fluid Mech.*, **714**, pp.5-23.
- KRIEG, M., & MOHSENI, K. 2008 Thrust characterization of a bioinspired vortex ring thruster for locomotion of underwater robots., *IEEE Journal of Oceanic Engineering*, **33(2)**, pp.123-132.
- LIM, T. T., & NICKELS, T. B. 1992 Instability and reconnection in the head-on collision of two vortex rings., *Nature*, **357**, pp.225-227.
- LEE, J., HSIEH, C., CHANG, C., & CHU, C. 2012 Vorticity forces on an impulsively started finite plate., *J. Fluid Mech.*, **694**, pp. 464-492.
- MAHULKAR, S., & ARAKERI, J. (2023). A self-propelling clapping body., *J. Fluid Mech.*, **971**, pp. A25.
- MAHULKAR, S., & ARAKERI, J. (2024). Contrasting flow dynamics between stationary and moving clapping bodies., *Physical Review Fluids*, **9(11)**, pp. 114702.
- MARTIN, N., ROH, C., IDREES, S., & GHARIB, M. 2017 To flap or not to flap: comparison between flapping and clapping propulsions., *J. Fluid Mech.*, 822.
- MELANDER, M. V., & HUSSAIN, F. 1989 Cross-linking of two antiparallel vortex tubes., *Physics of Fluids A: Fluid Dynamics*, **1(4)**, pp. 633-636.
- NEWMAN, J. N. 1977 Marine hydrodynamics, *The MIT press.*, pp.132-135.
- NICHOLS, J., MOSLEMI, A., & KRUEGER, P. 2008 Performance of a self-propelled pulsed-jet vehicle., *In 38th Fluid Dynamics Conference and Exhibit*, p. 3720.
- SULLIVAN, I. S., NIEMELA, J. J., HERSHBERGER, R. E., BOLSTER, D., & DONNELLY, R. J. (2008). Dynamics of thin vortex rings., *J. Fluid Mech.*, **609**, pp. 319-347.
- NICOLE W. XU, N. W. & DABIRI, J. O. 2020 Low-power microelectronics embedded in live jellyfish enhance propulsion., *Sci. Adv.*, **6(5)**, p. eaaz3194.